Analysis techniques

(applied to non-linear dynamics)

Yannis PAPAPHILIPPOU

Accelerator and Beam Physics group, Beams Department, CERN

and Physics Department Aristotelian University of Thessaloniki

CERN Accelerator School

11-23 November 2018

Thessaloniki, Greece

ΑΡΙΣΤΟΤΕΛΕΙΟ
ΠΑΝΕΠΙΣΤΗΜΙΟ
ΘΕΣΣΑΛΟΝΙΚΗΣ

Chaos detection methods

- Computing/measuring **dynamic aperture** (DA) or particle survival

A. Chao et al., PRL 61, 24, 2752, 1988;
F. Willeke, PAC95, 24, 109, 1989.

- Computation of Lyapunov exponents

F. Schmidt, F. Willeke and F. Zimmermann, PA, 35, 249, 1991;
M. Giovannozi, W. Scandale and E. Todesco, PA 56, 195, 1997

- Variance of unperturbed action (a la Chirikov)

B. Chirikov, J. Ford and F. Vivaldi, AIP CP-57, 323, 1979
J. Tennyson, SSC-155, 1988;
J. Irwin, SSC-233, 1989

- Fokker-Planck diffusion coefficient in actions

T. Sen and J.A. Elisson, PRL 77, 1051, 1996

- **Frequency map analysis**

Dynamic aperture

Dynamic Aperture

- The most direct way to evaluate the non-linear dynamics performance of a ring is the computation of **Dynamic Aperture**
- Particle motion due to multi-pole errors is generally non-bounded, so chaotic particles can **escape to infinity**
- This is not true for all non-linearities (e.g. the beam-beam force)
- Need a **symplectic** tracking code to follow particle trajectories (a lot of initial conditions) for a **number of turns** (depending on the given problem) until the particles start getting lost. This **boundary** defines the **Dynamic aperture**
- As multi-pole errors may not be completely known, one has to track through **several machine models** built by **random distribution** of these errors
- One could start with 4D (only transverse) tracking but certainly needs to simulate 5D (constant energy deviation) and finally 6D (synchrotron motion included)

Dynamic Aperture plots

- Dynamic aperture plots show the maximum initial values of stable trajectories in x-y coordinate space at a particular point in the lattice, for a range of energy errors.
  - The beam size can be shown on the same plot.
  - Generally, the goal is to allow some significant margin in the design - the measured dynamic aperture is often smaller than the predicted dynamic aperture.

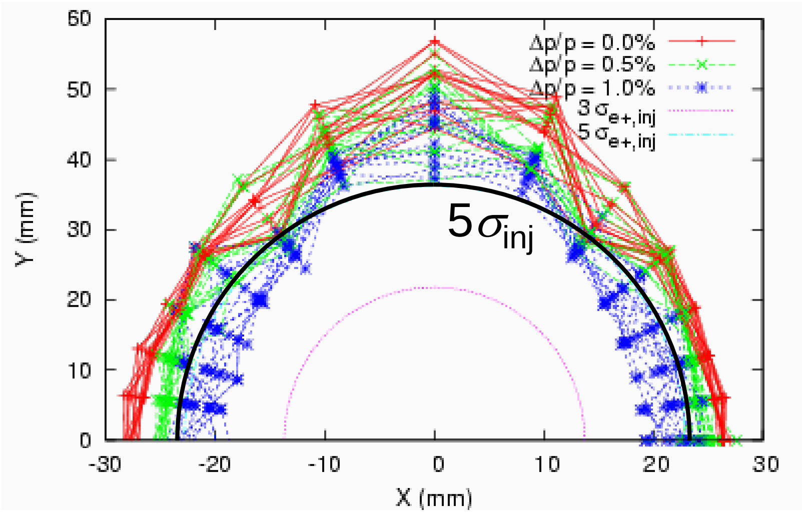

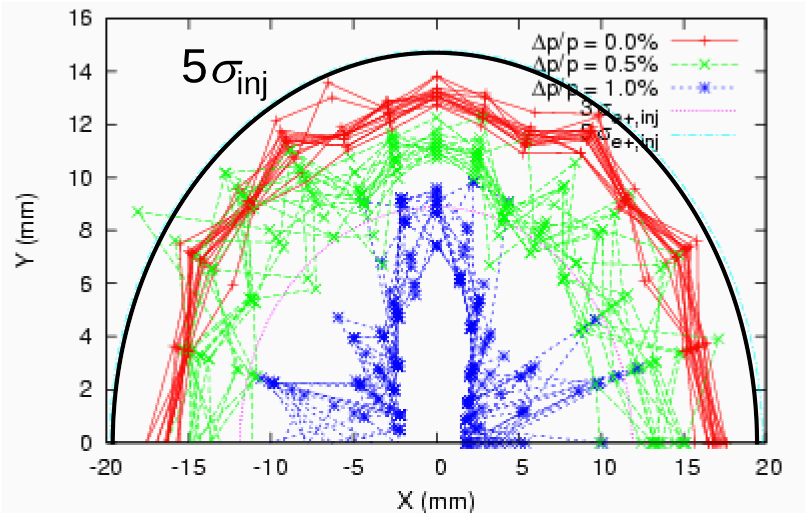

Dynamic aperture including damping

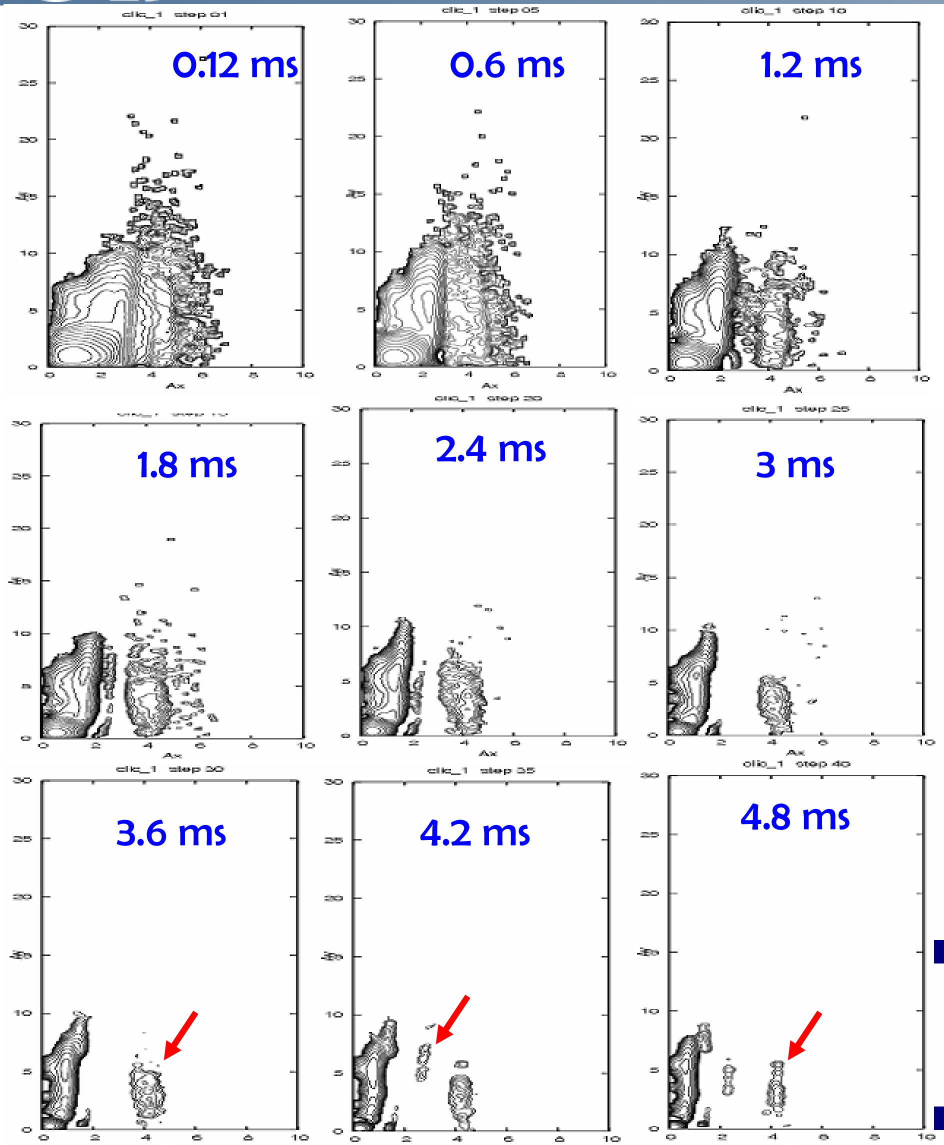

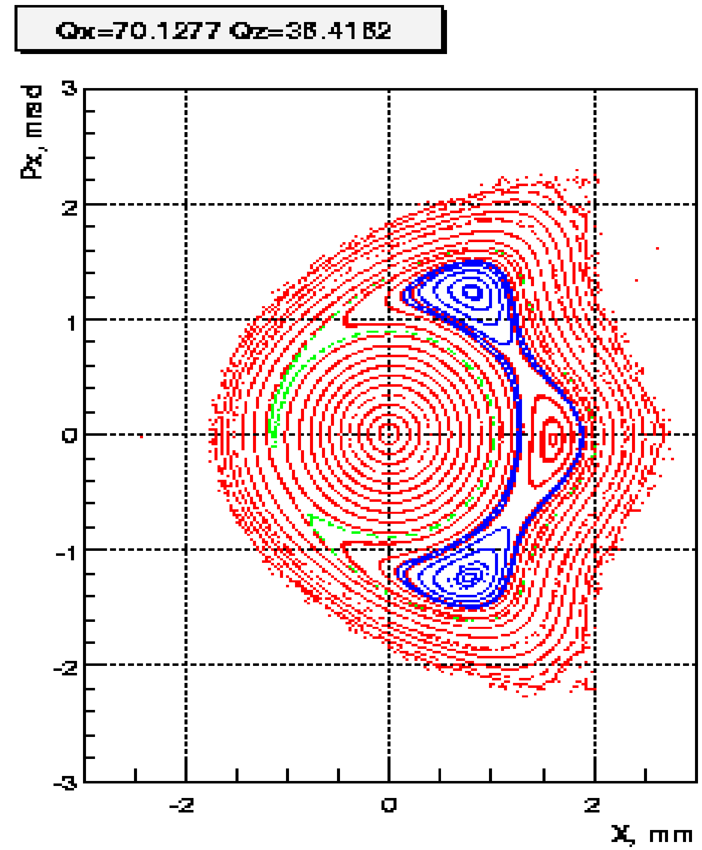

- Including radiation damping and excitation shows that 0.7% of the particles are lost during the damping
- Certain particles seem to damp away from the beam core, on resonance islands

DA scanning for the LHC

- **Min. Dynamic Aperture (DA)** with **intensity** vs **crossing angle**, for **nominal optics** (**β^*= 40 cm**) and **BCMS** beam (**2.5 µm** emittance), 15 units of chromaticity
- For **1.1×10^{11} p**
  - At **$\theta_c/2$ = 185 µrad** (~**12 σ** separation), DA around **6 σ (good lifetime observed)**
  - At **$\theta_c/2$ = 140 µrad** (~**9 σ** separation), DA below **5 σ (reduced lifetime observed)**
  - **Improvement** for low octupoles, low chromaticity and WP optimisation (observed in **operation**)

D.Pellegrini

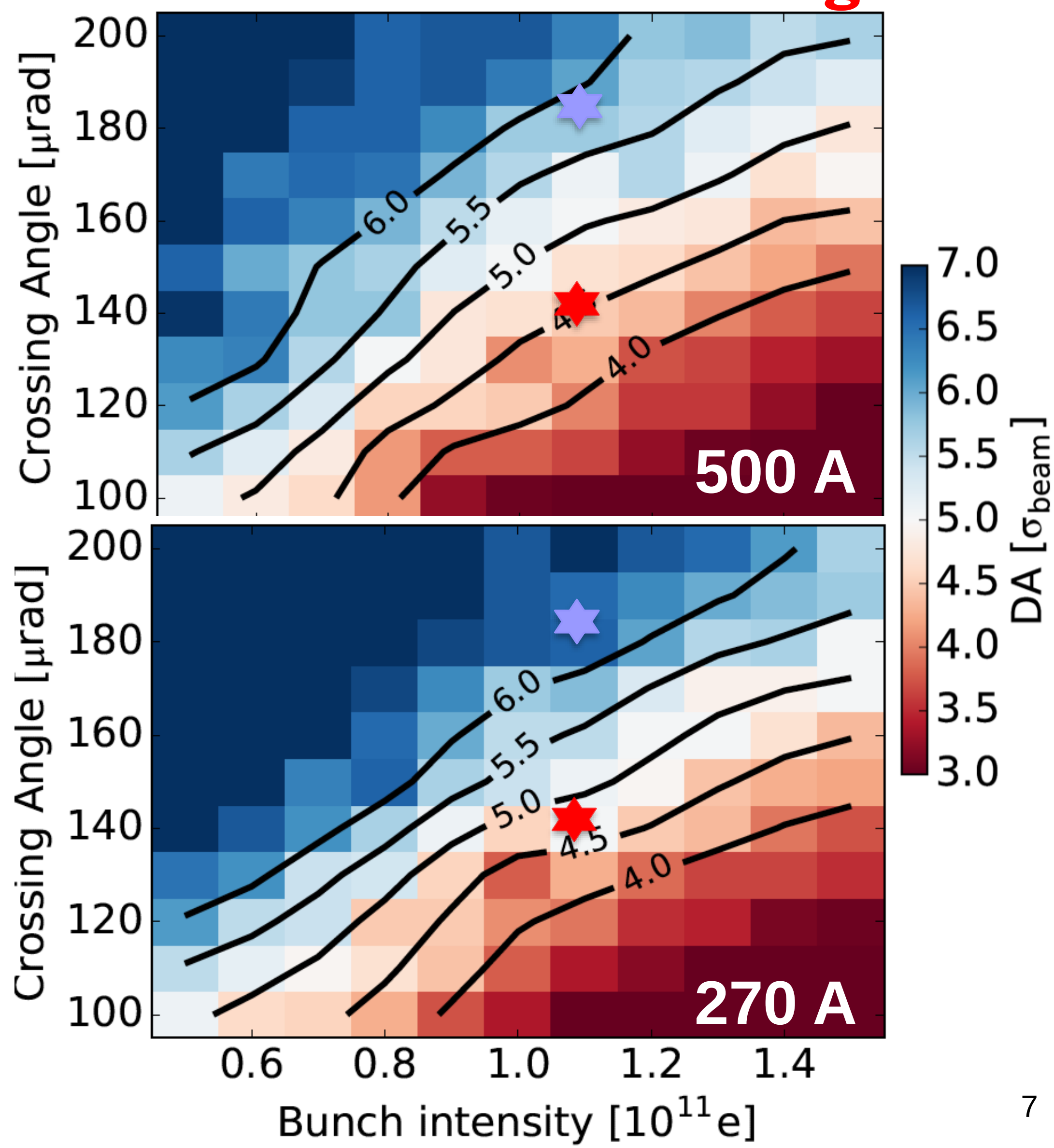

- MOGA –Multi Objective Genetic Algorithms are being recently used to optimise linear but also non-linear dynamics of electron low emittance storage rings
- Use knobs quadrupole strengths, chromaticity sextupoles and correctors with some constraints
- Target ultra-low horizontal emittance, increased lifetime and high dynamic aperture

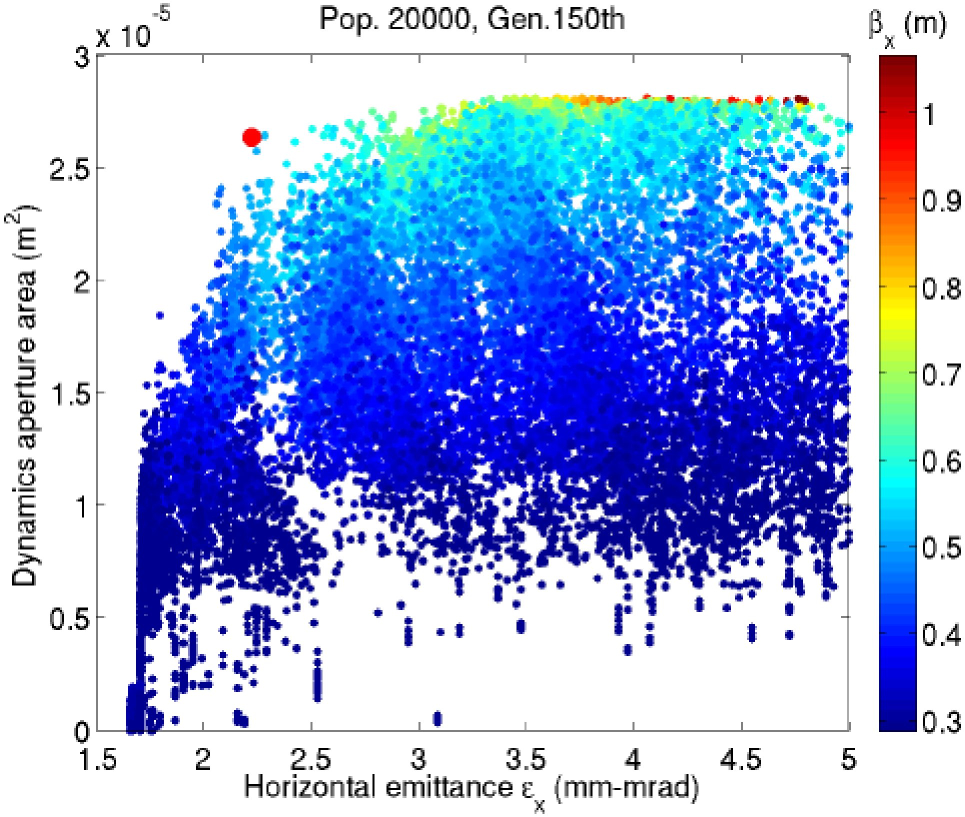

Measuring Dynamic Aperture

- During LHC design phase, DA target was 2x higher than collimator position, due to statistical fluctuation, finite mesh, linear imperfections, short tracking time, multi-pole time dependence, ripple and a 20% safety margin
- Better knowledge of the model led to good agreement between measurements and simulations for actual LHC
- Necessity to build an accurate magnetic model (from beam based measurements)

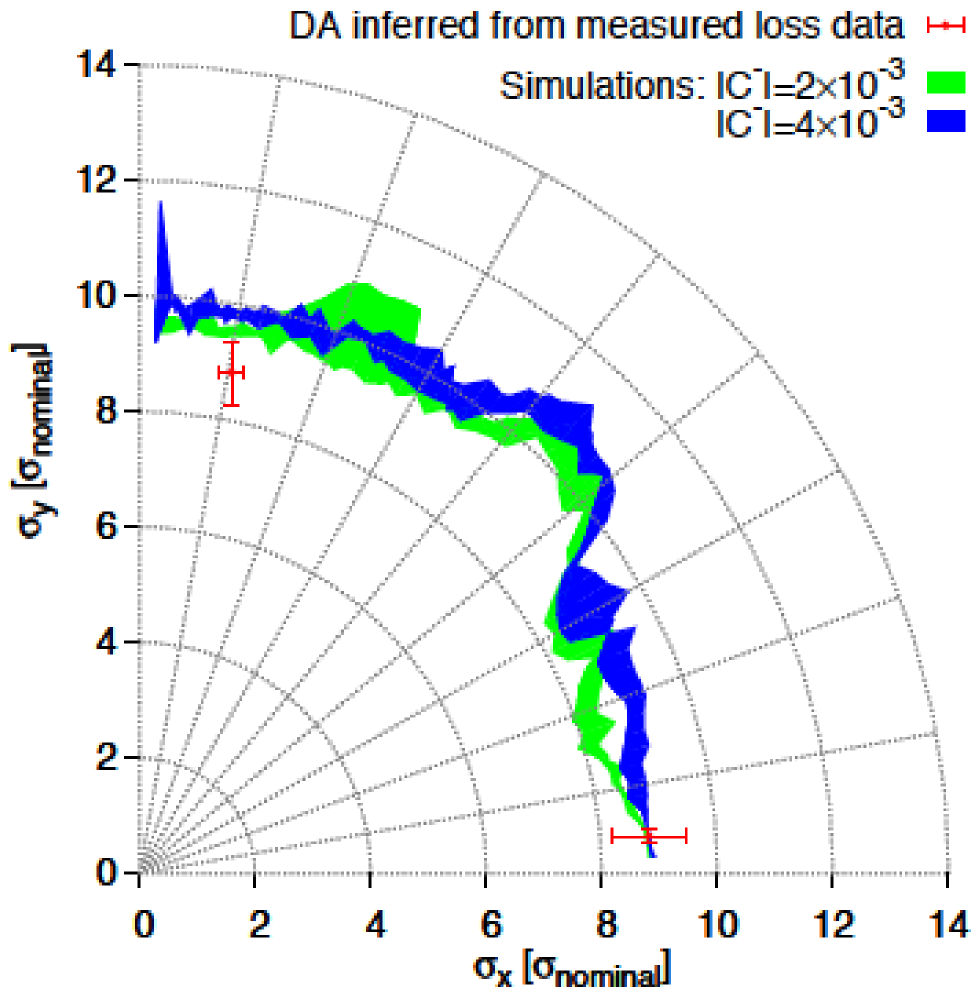

E.Mclean, PhD thesis, 2014

DA guiding machine performance

- B1 suffering from lower lifetime in the LHC
- DA simulations predicted the required adjustment
- Fine-tune scan performed and applied in operation, solving B1 lifetime problem

D. Pellegrini et al., 2016

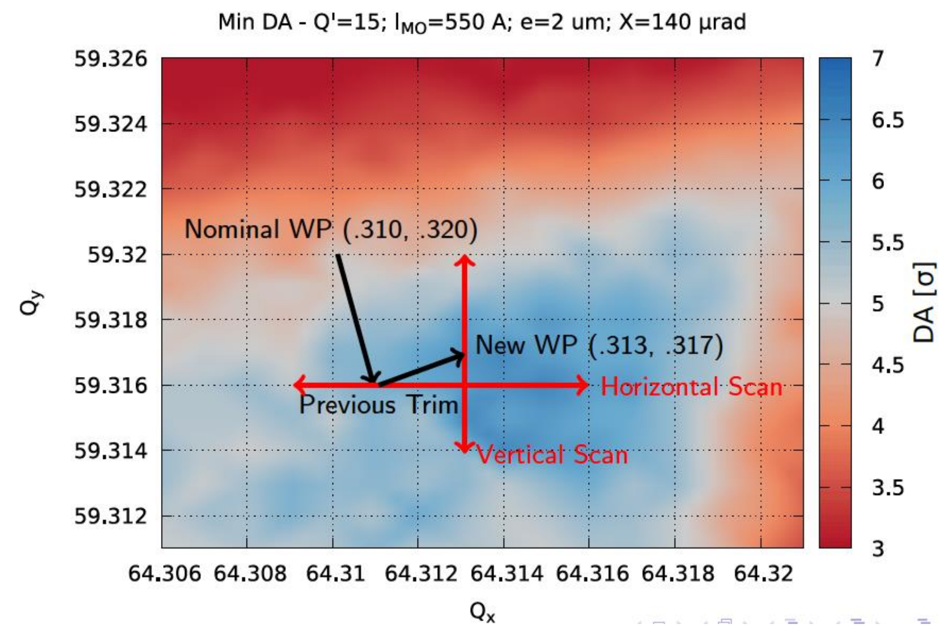

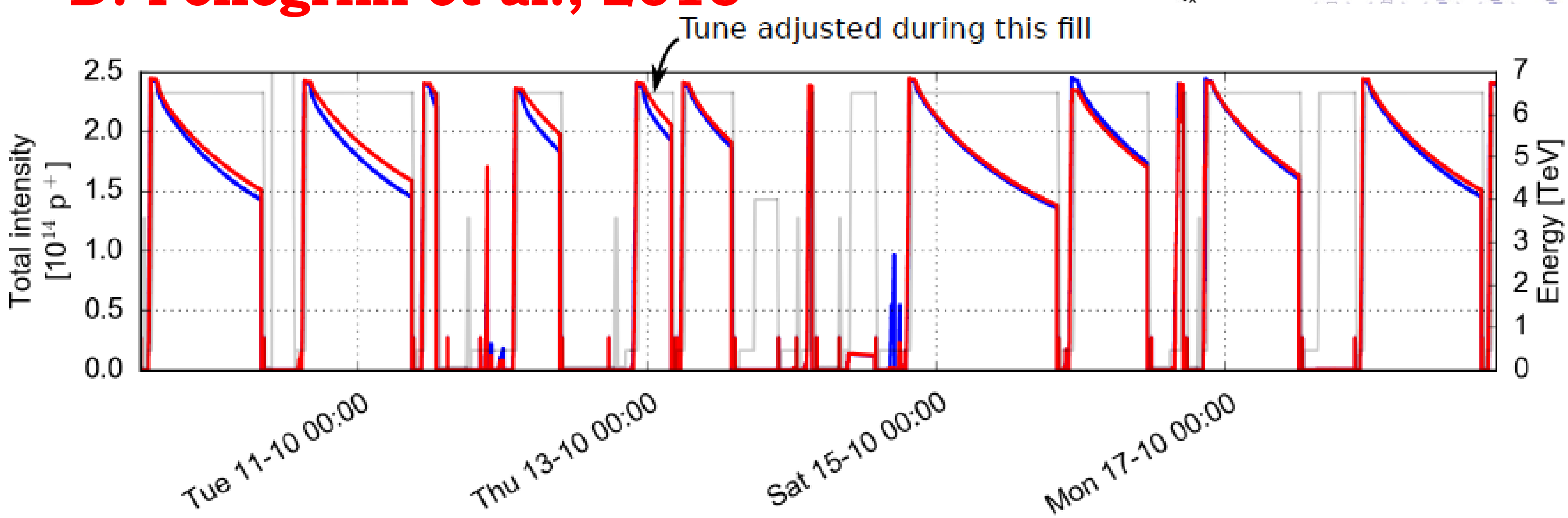

HL-LHC operational scenario

- Reduction of **crossing angle** at **constant luminosity**, reduces **pileup density** (by elongating the luminous region) and **triplet irradiation**

YP, N. Karastathis and D. Pellegrini et al., 2018

Relaxed DA

Aggressive DA

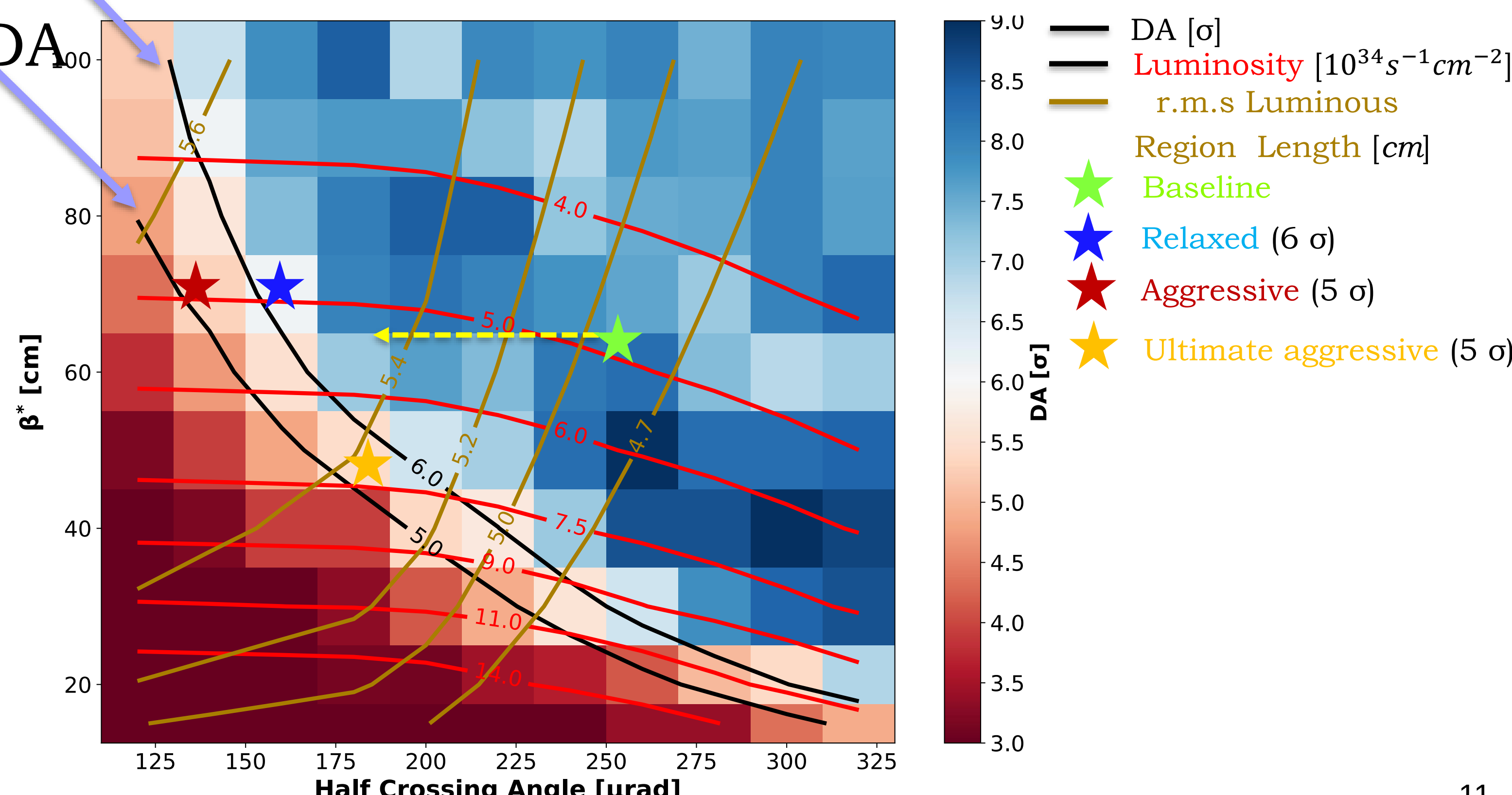

Lyapunov exponent

Lyapunov exponent

- Chaotic motion implies **sensitivity** to **initial condition**
- Two infinitesimally close **chaotic trajectories** in phase space with initial difference $\delta\mathbf{Z}_0$ will end-up diverging with rate

$$|\delta\mathbf{Z}(t)| \approx e^{\lambda t}|\delta\mathbf{Z}_0|$$

  with λ the maximum **Lyapunov exponent**
- There is as many exponents as the phase space dimensions (Lyapunov spectrum)
- The largest one is the **Maximal Lyapunov exponent** (MLE) is defined as

$$\lambda = \lim_{t\to\infty} \lim_{\delta\mathbf{Z}_0\to 0} \frac{1}{t} \ln \frac{|\delta\mathbf{Z}(t)|}{|\delta\mathbf{Z}_0|}$$

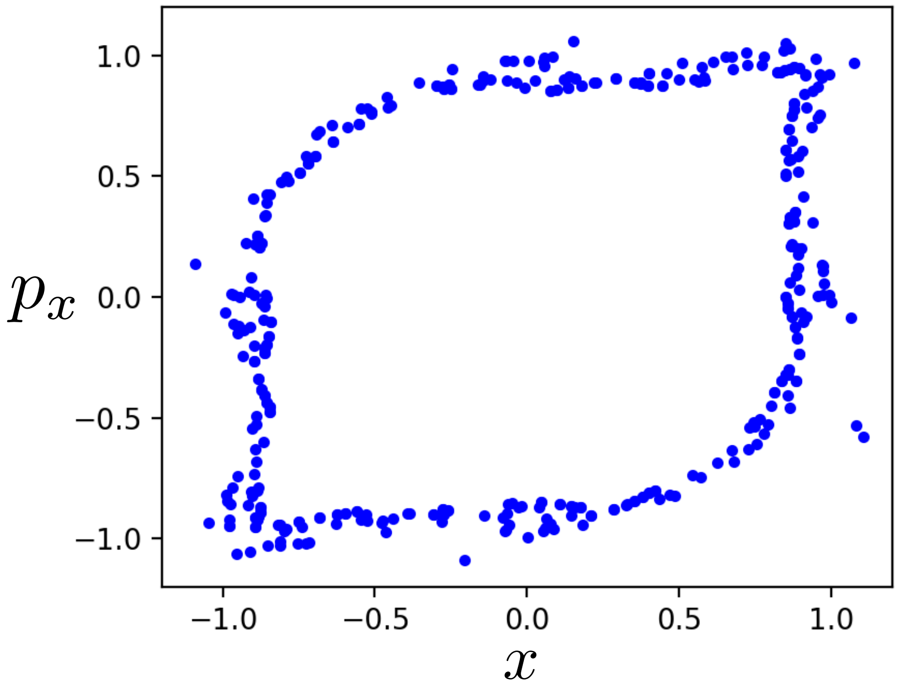

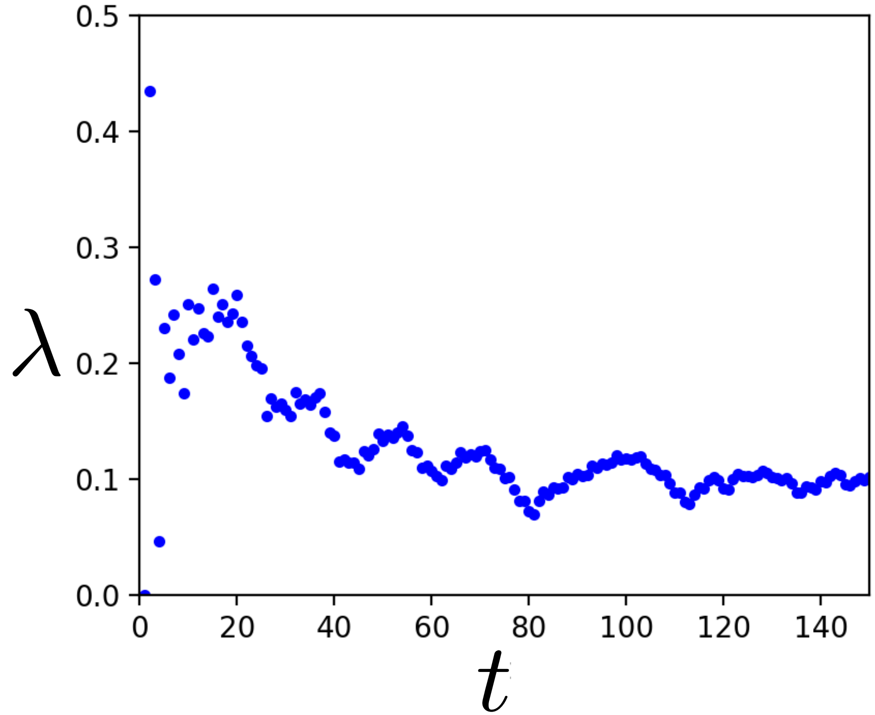

- Maximum Lyapounov exponent converges towards a **positive value** for a chaotic orbit

$$\lambda = \lim_{t\to\infty} \lim_{\delta \mathbf{Z}_0 \to 0} \frac{1}{t} \ln \frac{|\delta \mathbf{Z}(t)|}{|\delta \mathbf{Z}_0|}$$

Lyapunov exponent: regular orbit

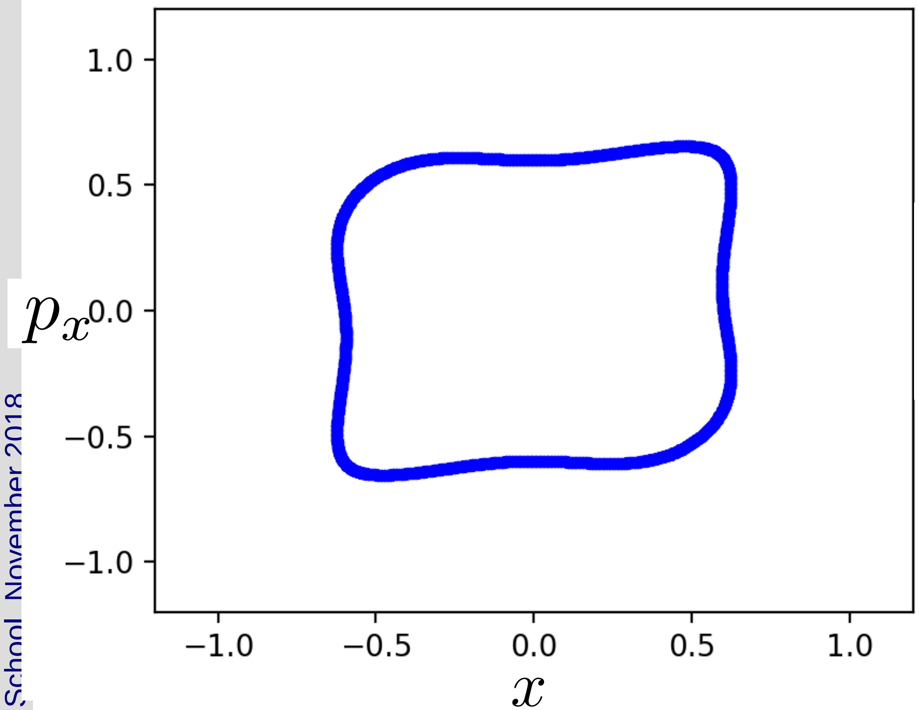

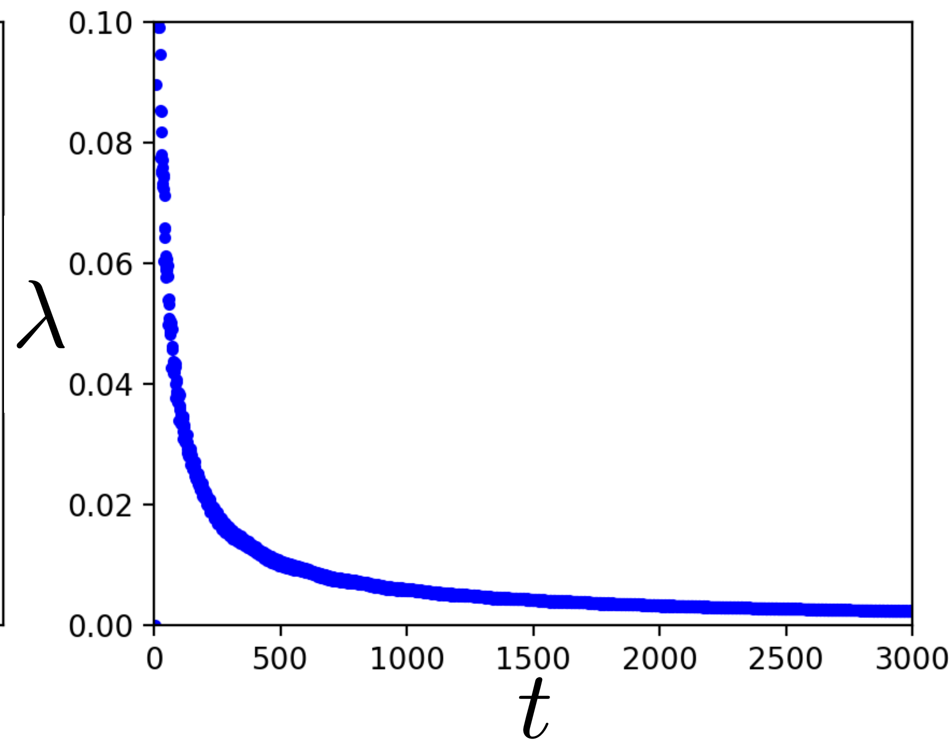

- Maximum Lyapounov exponent converges towards **zero** for a chaotic orbit

$$\lambda = \lim_{t \to \infty} \lim_{\delta \mathbf{Z}_0 \to 0} \frac{1}{t} \ln \frac{|\delta \mathbf{Z}(t)|}{|\delta \mathbf{Z}_0|}$$

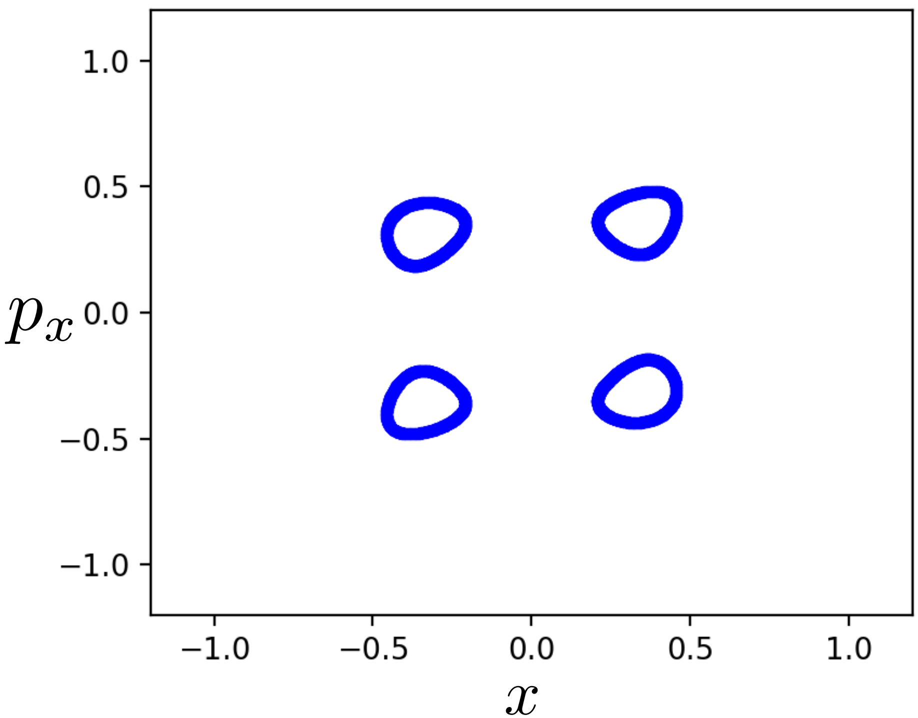

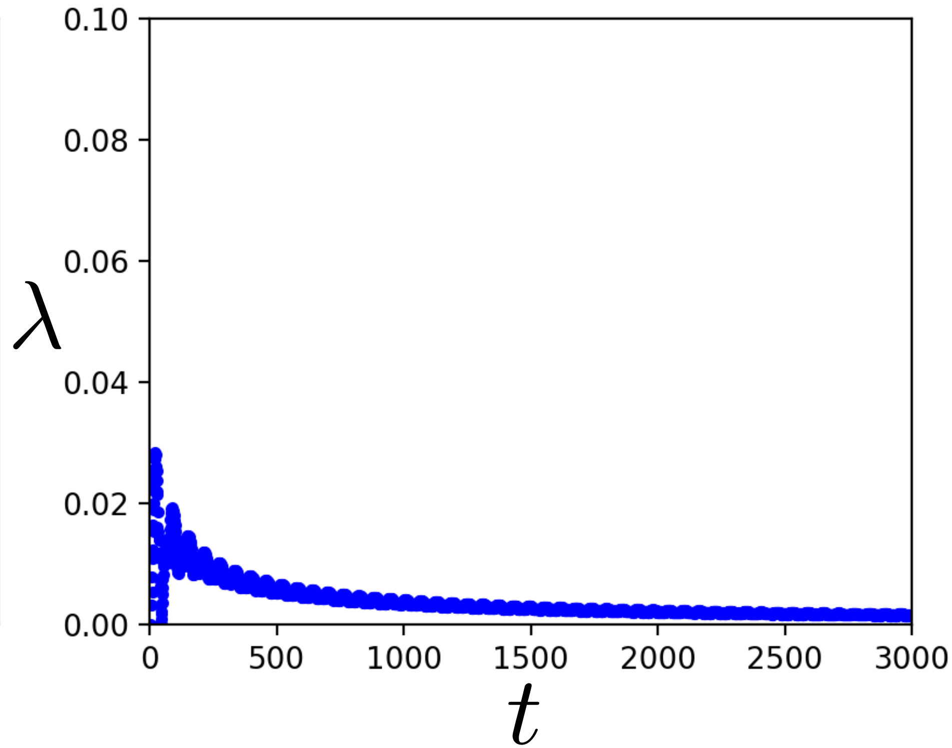

- Maximum Lyapounov exponent converges more slowly towards **zero** for a resonant orbit

$$\lambda = \lim_{t \to \infty} \lim_{\delta \mathbf{Z}_0 \to 0} \frac{1}{t} \ln \frac{|\delta \mathbf{Z}(t)|}{|\delta \mathbf{Z}_0|}$$

Lyapunov exponent: regular orbit

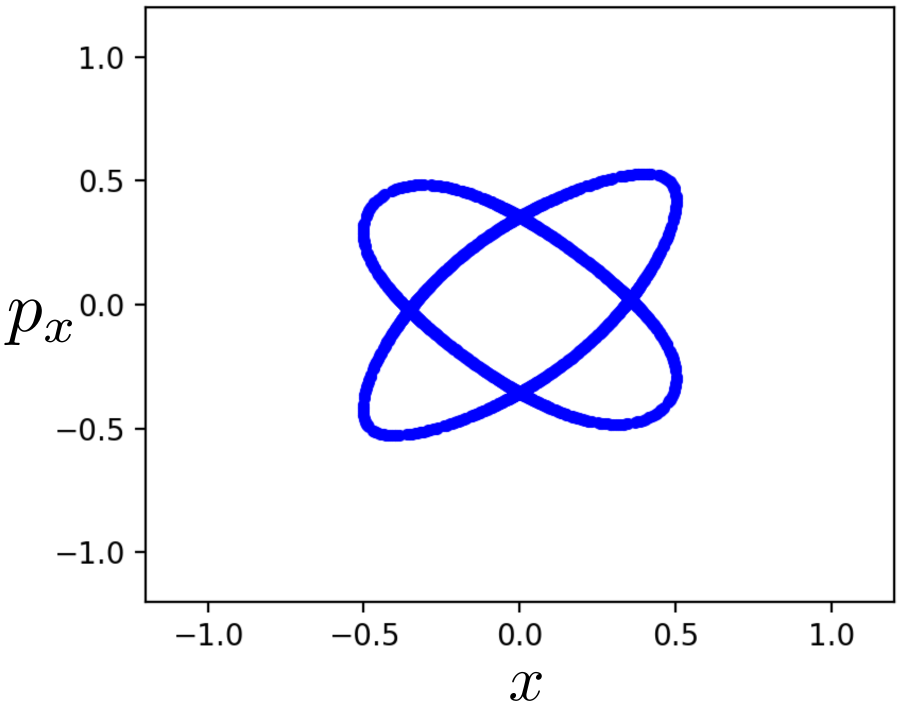

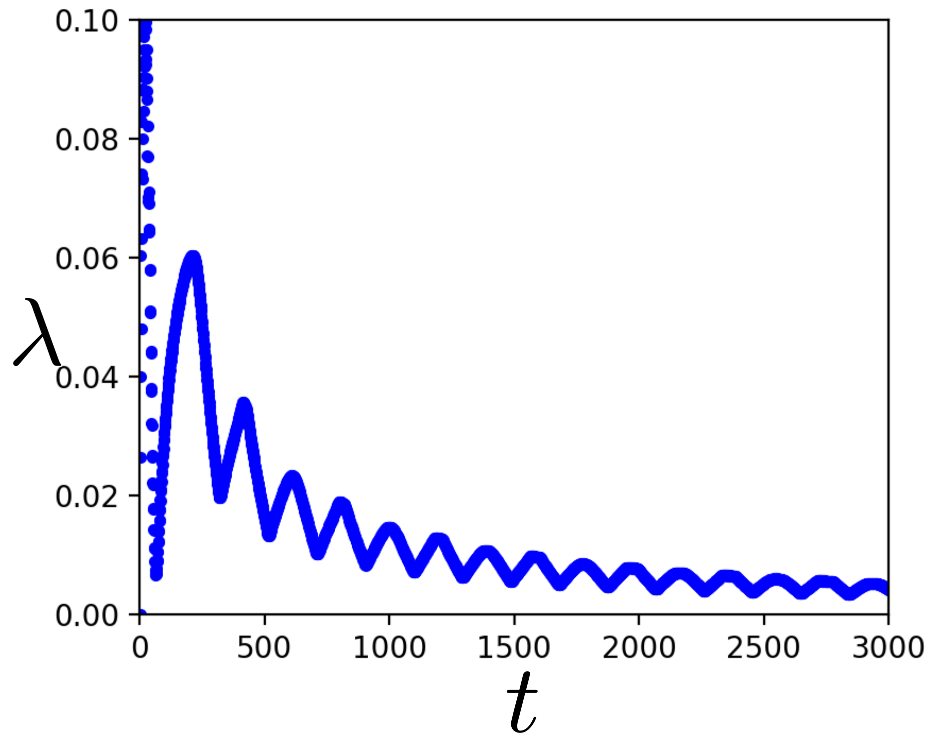

- Maximum Lyapounov exponent converges more slowly towards **zero** for a resonant orbit, in particular close to the separatrix

$$\lambda = \lim_{t\to\infty} \lim_{\delta \mathbf{Z}_0 \to 0} \frac{1}{t} \ln \frac{|\delta \mathbf{Z}(t)|}{|\delta \mathbf{Z}_0|}$$

Frequency Map Analysis

Frequency map analysis

- Frequency Map Analysis (FMA) is a numerical method which springs from the studies of J. Laskar (Paris Observatory) putting in evidence the chaotic motion in the Solar Systems
- FMA was successively applied to several dynamical systems
  - Stability of Earth Obliquity and climate stabilization (Laskar, Robutel, 1993)
  - 4D maps (Laskar 1993)
  - Galactic Dynamics (Y.P and Laskar, 1996 and 1998)
  - Accelerator beam dynamics: lepton and hadron rings (Dumas, Laskar, 1993, Laskar, Robin, 1996, Y.P, 1999, Nadolski and Laskar 2001)

Motion on torus

- Consider an integrable Hamiltonian system of the usual form

$$H(\boldsymbol{J},\boldsymbol{\varphi},\theta) = H_0(\mathbf{J})$$

- Hamilton's equations give

$$\dot{\phi}_j = \frac{\partial H_0(\mathbf{J})}{\partial J_j} = \omega_j(\mathbf{J}) \Rightarrow \phi_j = \omega_j(\mathbf{J})t + \phi_{j0}$$

$$\dot{J}_j = -\frac{\partial H_0(\mathbf{J})}{\partial \phi_j} = 0 \Rightarrow J_j = \text{const.}$$

- The actions define the surface of an invariant torus
- In complex coordinates the motion is described by

$$\zeta_j(t) = J_j(0)e^{i\omega_j t} = z_{j0}e^{i\omega_j t}$$

- For a **non-degenerate** system $\det\left|\frac{\partial\omega(J)}{\partial J}\right| = \det\left|\frac{\partial^2 H_0(J)}{\partial J^2}\right| \neq 0$ there is a one-to-one correspondence between the actions and the frequency, a frequency map can be defined parameterizing the tori in the frequency space

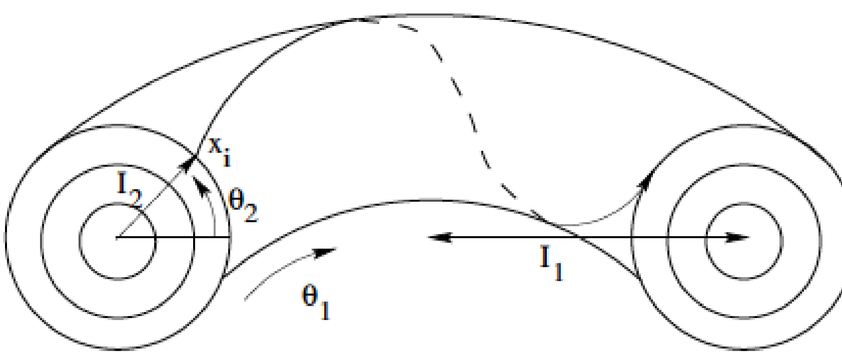

$$F: \quad (\mathbf{I}) \longrightarrow (\omega)$$

Quasi-periodic motion

- If a transformation is made to some new variables

$$\zeta_j = I_j e^{i\theta_j t} = z_j + \epsilon G_j(\mathbf{z}) = z_j + \epsilon \sum_{\mathbf{m}} c_{\mathbf{m}} z_1^{m_1} z_2^{m_2} \ldots z_n^{m_n}$$

- The system is still integrable but the tori are distorted
- The motion is then described by

$$\zeta_j(t) = z_{j0} e^{i\omega_j t} + \sum_{\mathbf{m}} a_{\mathbf{m}} e^{i\,(\mathbf{m}\cdot\omega)\,t}$$

i.e.

a quasi-periodic function of time, with

$$a_{\mathbf{m}} = \epsilon\, c_{\mathbf{m}} z_{10}^{m_1} z_{20}^{m_2} \ldots z_{n0}^{m_n} \text{ and } \mathbf{m}\cdot\omega = m_1\omega_1 + m_2\omega_2 + \cdots + m_n\omega_n$$

- For a non-integrable Hamiltonian, $H(\mathbf{I},\theta) = H_0(\mathbf{I}) + \epsilon H'(\mathbf{I},\theta)$ and especially if the perturbation is small, most tori persist (**KAM** theory)
- In that case, the motion is still quasi-periodic and a frequency map can be built
- The **regularity** (or not) of the map reveals stable (or chaotic) motion

Building the frequency map

- When a quasi-periodic function $f(t) = q(t) + ip(t)$ in the complex domain is given numerically, it is possible to recover a quasi-periodic approximation

$$f'(t) = \sum_{k=1}^{N} a'_k e^{i\omega'_k t}$$

  in a very precise way over a finite time span $[-T, T]$ several orders of magnitude more precisely than simple Fourier techniques
- This approximation is provided by the Numerical Analysis of Fundamental Frequencies – **NAFF** algorithm
- The frequencies ω'_k and complex amplitudes a'_k are computed through an iterative scheme.

The NAFF algorithm

- The first frequency ω_1' is found by the location of the maximum of

$$\phi(\sigma) = \langle f(t), e^{i\sigma t} \rangle = \frac{1}{2T}\int_{-T}^{T} f(t)e^{-i\sigma t}\chi(t)dt$$

where $\chi(t)$ is a weight function

- In most of the cases the Hanning window filter is used $\chi_1(t) = 1 + \cos(\pi t/T)$
- Once the first term $e^{i\omega_1' t}$ is found, its complex amplitude a_1' is obtained and the process is restarted on the remaining part of the function

$$f_1(t) = f(t) - a_1' e^{i\omega_1' t}$$

- The procedure is continued for the number of desired terms, or until a required precision is reached

Frequency determination

- The accuracy of a simple FFT even for a simple sinusoidal signal is not better than $|\nu - \nu_T| = \frac{1}{T}$
- Calculating the Fourier integral explicitly

$$\phi(\omega) = < f(t),\ e^{i\omega t} > = \frac{1}{T}\int_0^T f(t)\ e^{-i\omega t}\ dt$$

shows that the maximum lies in between the main peaks of the FFT

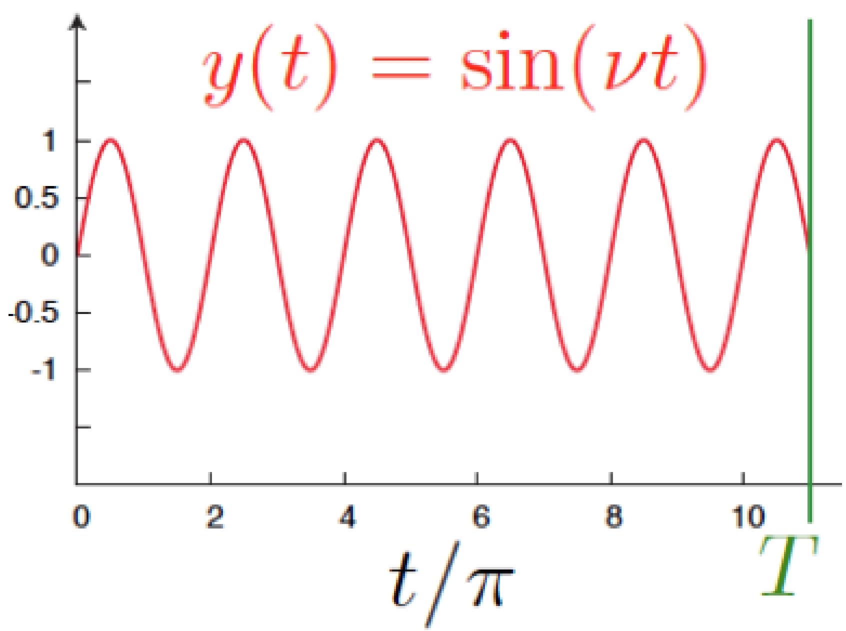

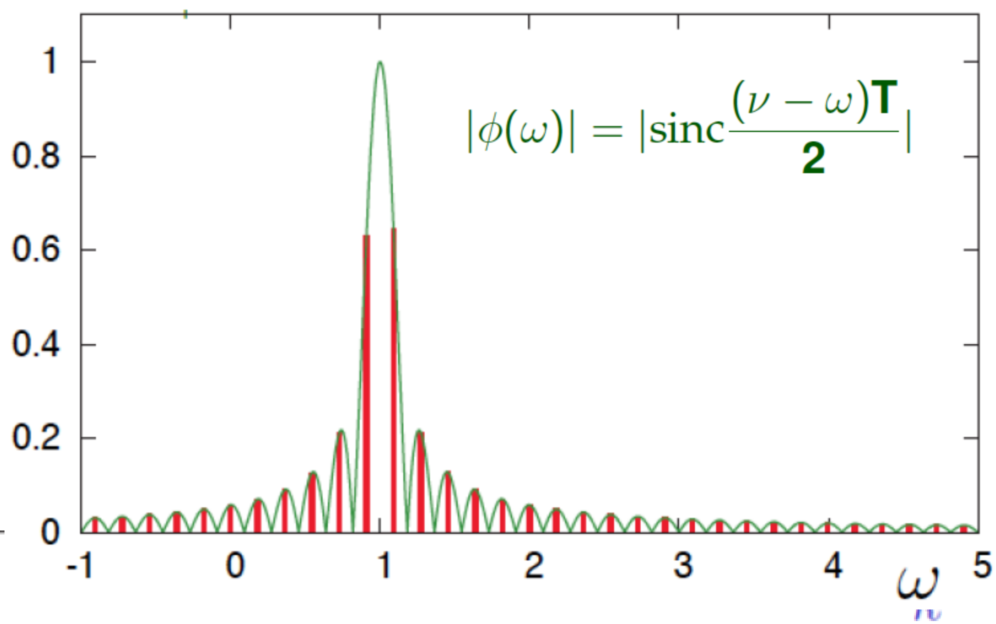

Frequency determination

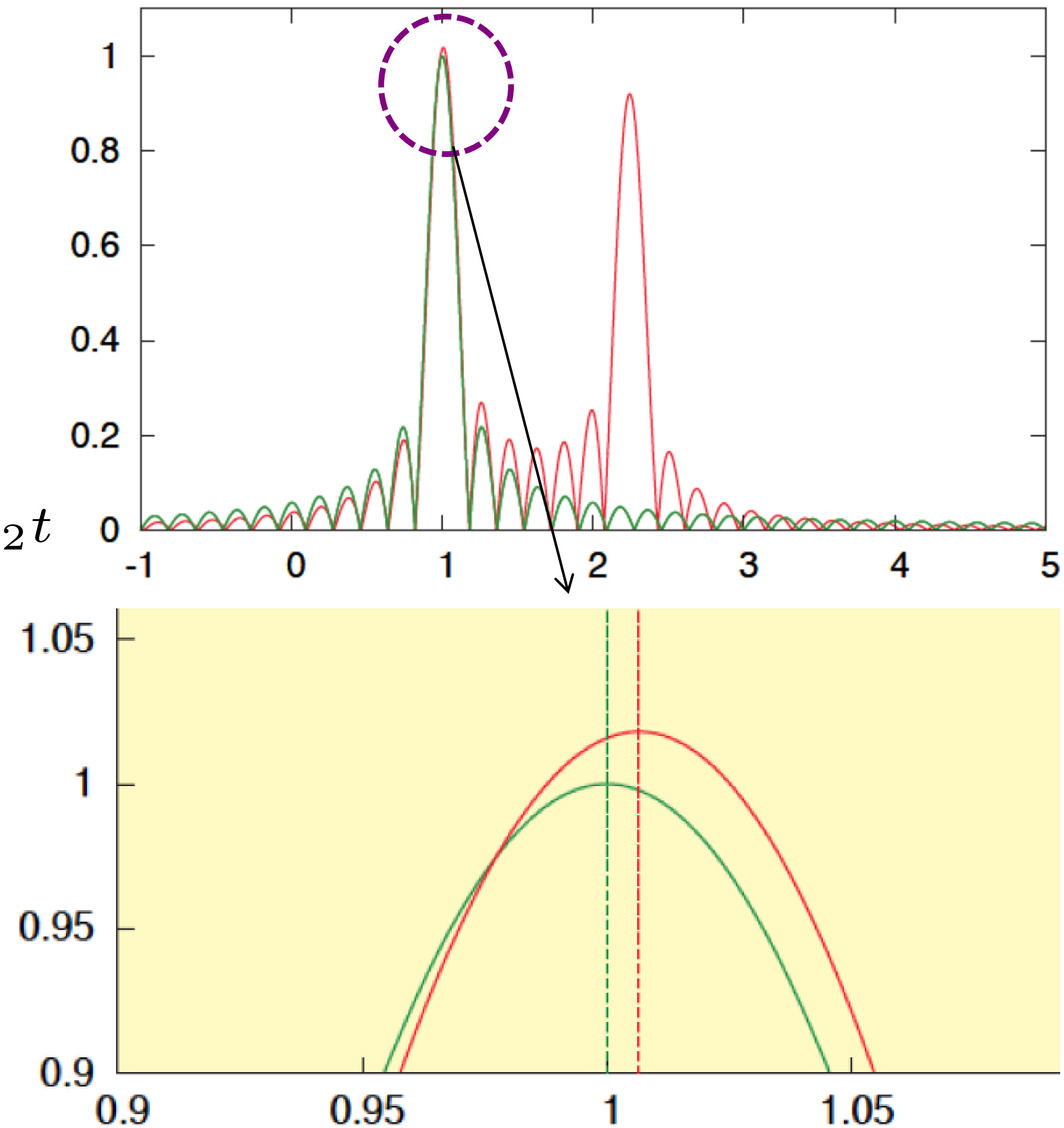

- A more complicated signal with two frequencies

$$f(t) = a_1 e^{i\omega_1 t} + a_2 e^{i\omega_2 t}$$

shifts slightly the maximum with respect to its real location

Window function

- A window function like the Hanning filter $\chi_1(t) = 1 + \cos(\pi t/T)$ kills side-lobs and allows a very accurate determination of the frequency

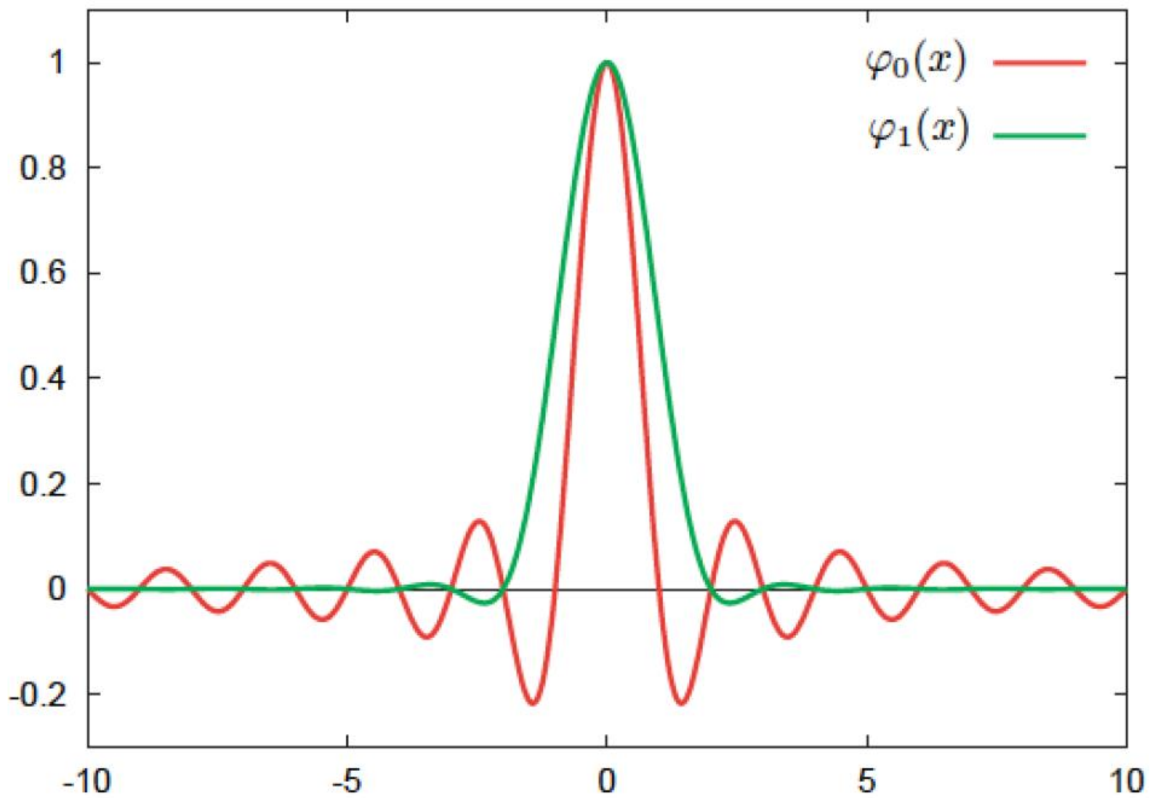

Precision of NAFF

- For a general window function of order p

$$\chi_p(t) = \frac{2^p (p!)^2}{(2p)!}(1+\cos \pi t)^p$$

Laskar (1996) proved a theorem stating that the solution provided by the NAFF algorithm converges asymptotically towards the real KAM quasi-periodic solution with precision

$$\nu_1 - \nu_1^T \propto \frac{1}{T^{2p+2}}$$

- In particular, for no filter (i.e. $p=0$) the precision is $\frac{1}{T^2}$, whereas for the Hanning filter ($p=1$), the precision is of the order of $\frac{1}{T^4}$

Aspects of the frequency map

- In the vicinity of a resonance the system behaves like a **pendulum**
- Passing through the **elliptic point** for a fixed angle, a **fixed frequency** (or rotation number) is observed
- Passing through the **hyperbolic point**, a **frequency jump** is observed

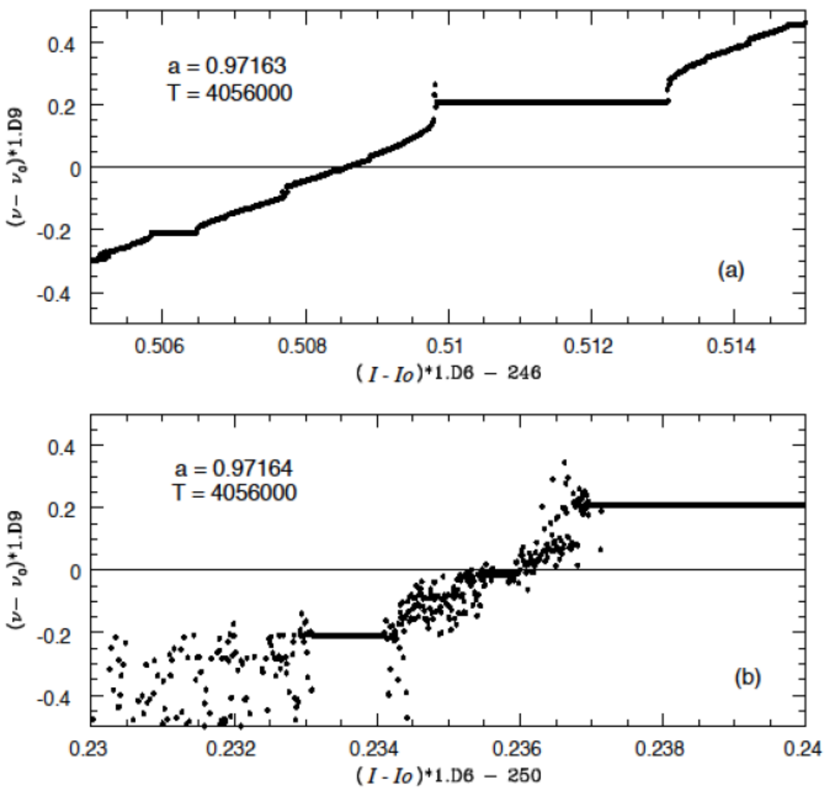

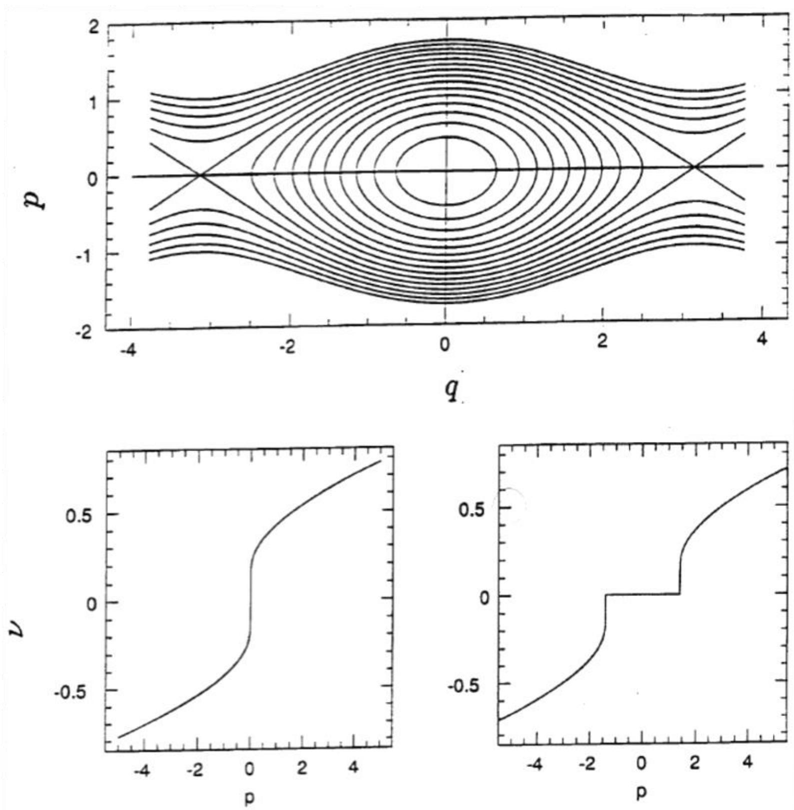

Example: Frequency map for BBLR

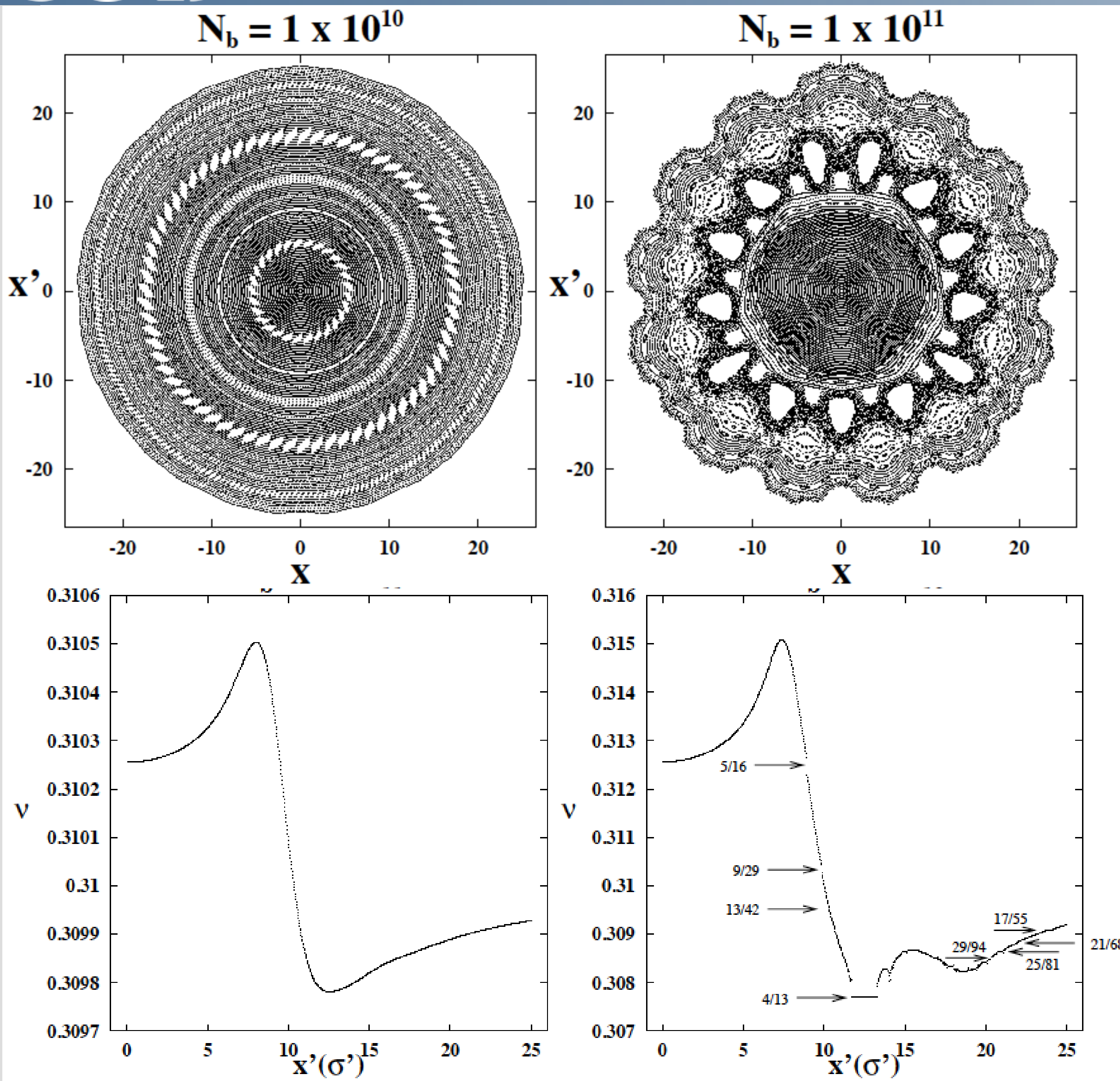

- Simple Beam-beam long range (BBLR) kick and a rotation

$$\begin{pmatrix} x \\ x' \end{pmatrix}_1 = \begin{pmatrix} \cos\mu & \beta^*\sin\mu \\ -\sin\mu/\beta^* & \cos\mu \end{pmatrix} \begin{pmatrix} x + f(x') \\ x' \end{pmatrix}_0 \qquad f(x') = K\left[\frac{1}{x'+\theta_c}\left(1-e^{-\frac{(x'+\theta_c)^2}{2{\sigma'_x}^2}}\right) - \frac{1}{\theta_c}\left(1-e^{-\frac{\theta_c^2}{2{\sigma'_x}^2}}\right)\right]$$

Example: Frequency map for BBLR

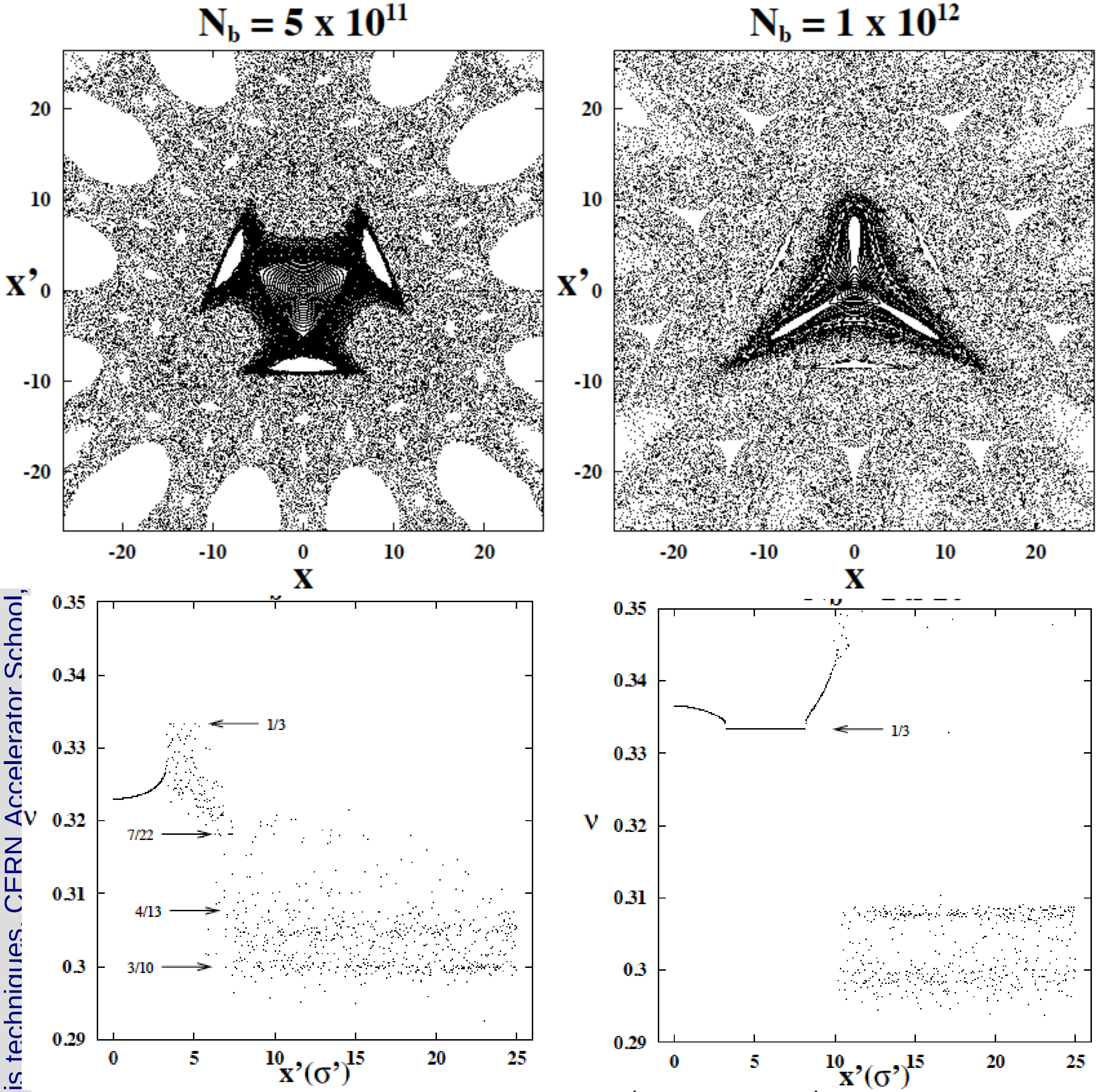

- Simple Beam-beam long range (BBLR) kick and a rotation

$$\begin{pmatrix} x \\ x' \end{pmatrix}_1 = \begin{pmatrix} \cos\mu & \beta^*\sin\mu \\ -\sin\mu/\beta^* & \cos\mu \end{pmatrix} \begin{pmatrix} x+f(x') \\ x' \end{pmatrix}_0 \quad f(x') = K\left[\frac{1}{x'+\theta_c}\left(1-e^{-\frac{(x'+\theta_c)^2}{2\sigma_x'^2}}\right) - \frac{1}{\theta_c}\left(1-e^{-\frac{\theta_c^2}{2\sigma_x'^2}}\right)\right]$$

Diffusion in frequency space

- For a **2 degrees of freedom** Hamiltonian system, the **frequency space** is a **line**, the tori are dots on this lines, and the **chaotic zones** are **confined** by the existing KAM tori
- For a system with 3 or more degrees of freedom, KAM tori are still represented by dots but do not prevent chaotic trajectories to diffuse

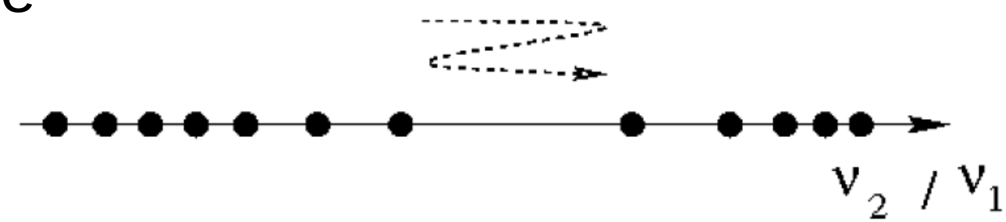

- This topological possibility of particles diffusing is called **Arnold diffusion**
- This diffusion is supposed to be extremely small in their vicinity, as tori act as effective barriers (**Nechoroshev theory**)

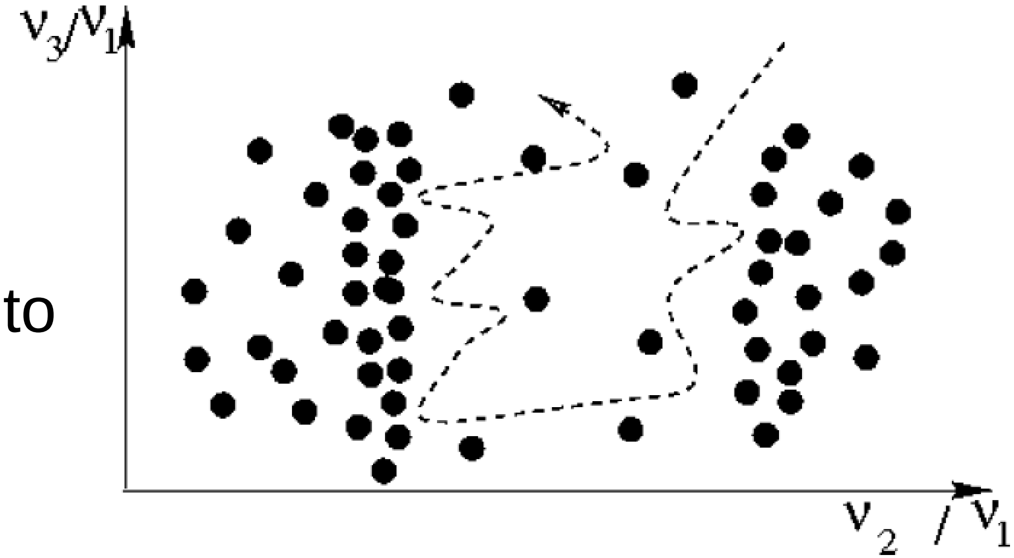

Building the frequency map

- Choose coordinates (x_i, y_i) with p_x and p_y=0
- Numerically integrate the phase trajectories through the lattice for sufficient number of turns
- Compute through NAFF Q_x and Q_y after sufficient number of turns
- Plot them in the tune diagram

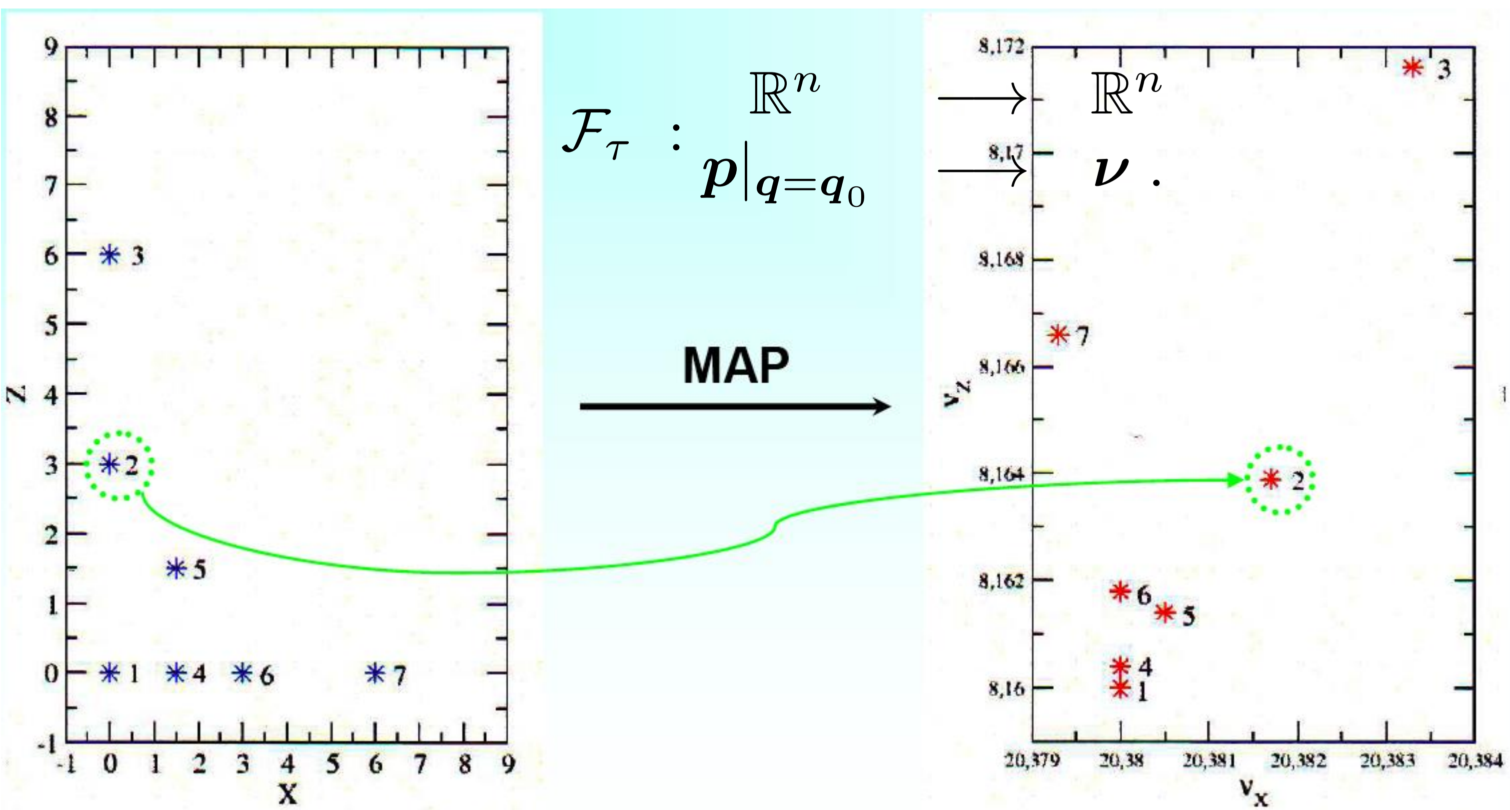

Example: Frequency maps for the LHC

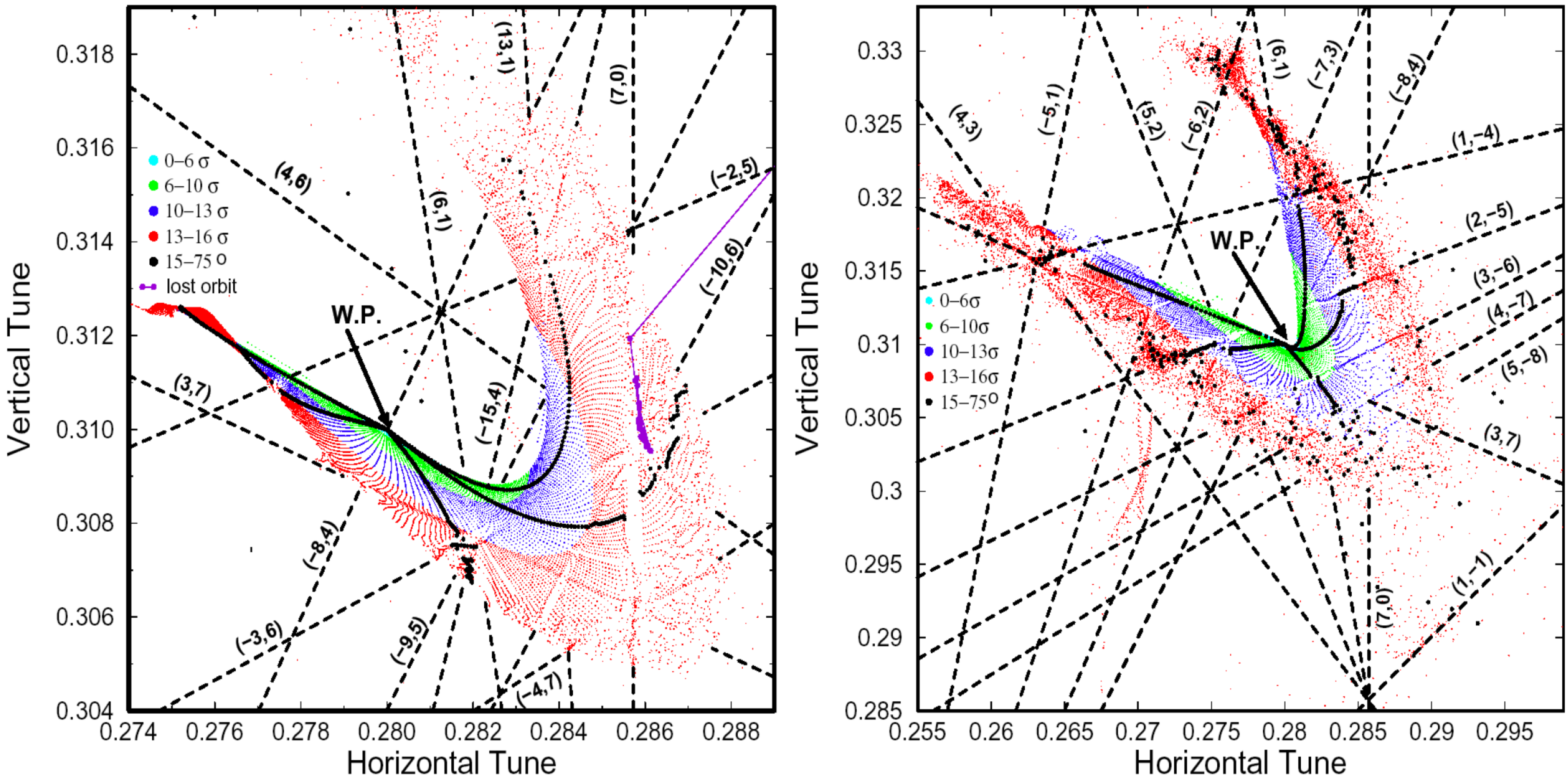

- Frequency maps for the target error table (left) and an increased random skew octupole error in the super-conducting dipoles (right)

- Calculate frequencies for two equal and successive time spans and compute frequency diffusion vector:

$$\boldsymbol{D}\big|_{t=\tau} = \boldsymbol{\nu}\big|_{t\in(0,\tau/2]} - \boldsymbol{\nu}\big|_{t\in(\tau/2,\tau]}$$

- Plot the initial condition space color-coded with the norm of the diffusion vector
- Compute a diffusion quality factor by averaging all diffusion coefficients normalized with the initial conditions radius

$$D_{QF} = \left\langle \frac{|\boldsymbol{D}|}{(I_{x0}^2 + I_{y0}^2)^{1/2}} \right\rangle_R$$

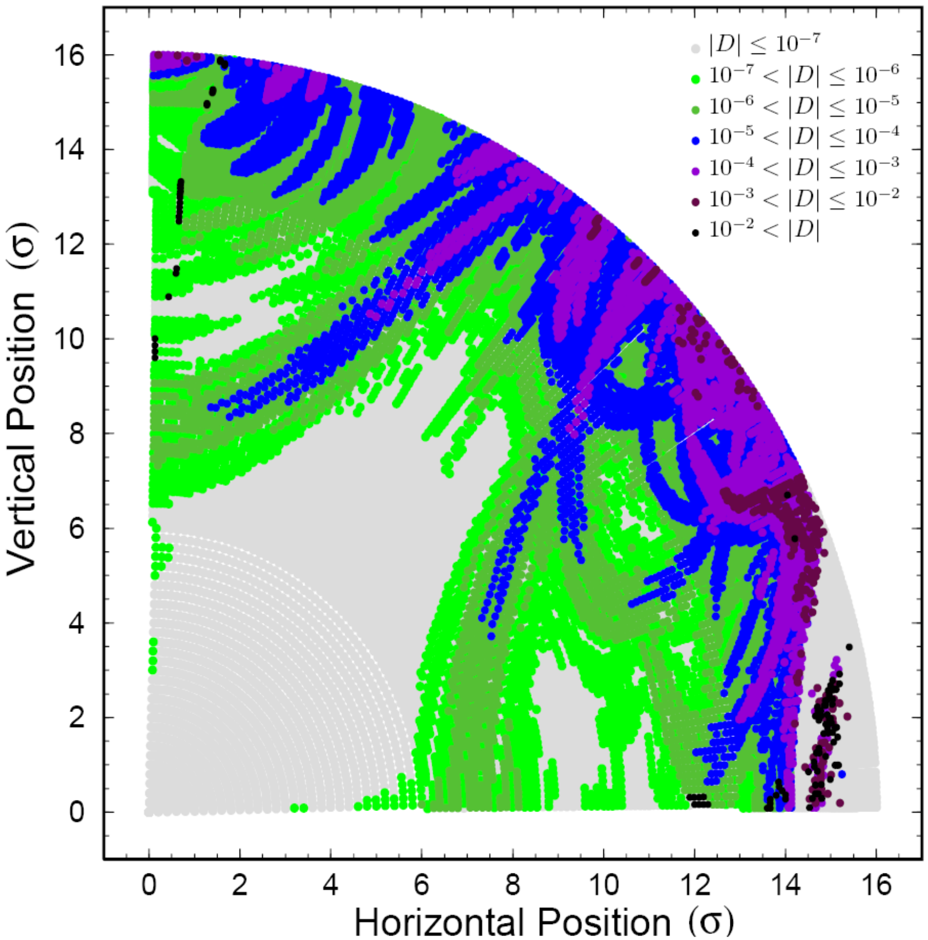

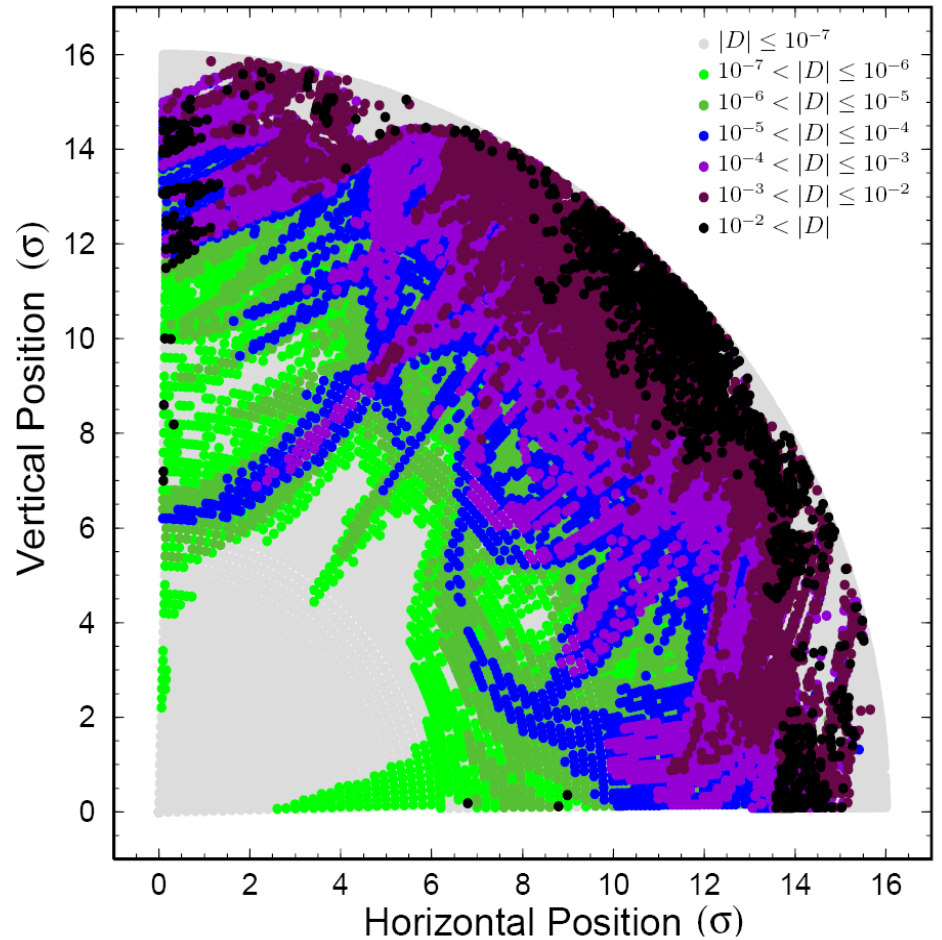

Diffusion maps for the target error table (left) and an increased random skew octupole error in the super-conducting dipoles (right)

Example: Frequency Map for the ESRF

- All dynamics represented in these two plots
- Regular motion represented by blue colors (close to zero amplitude particles or working point)

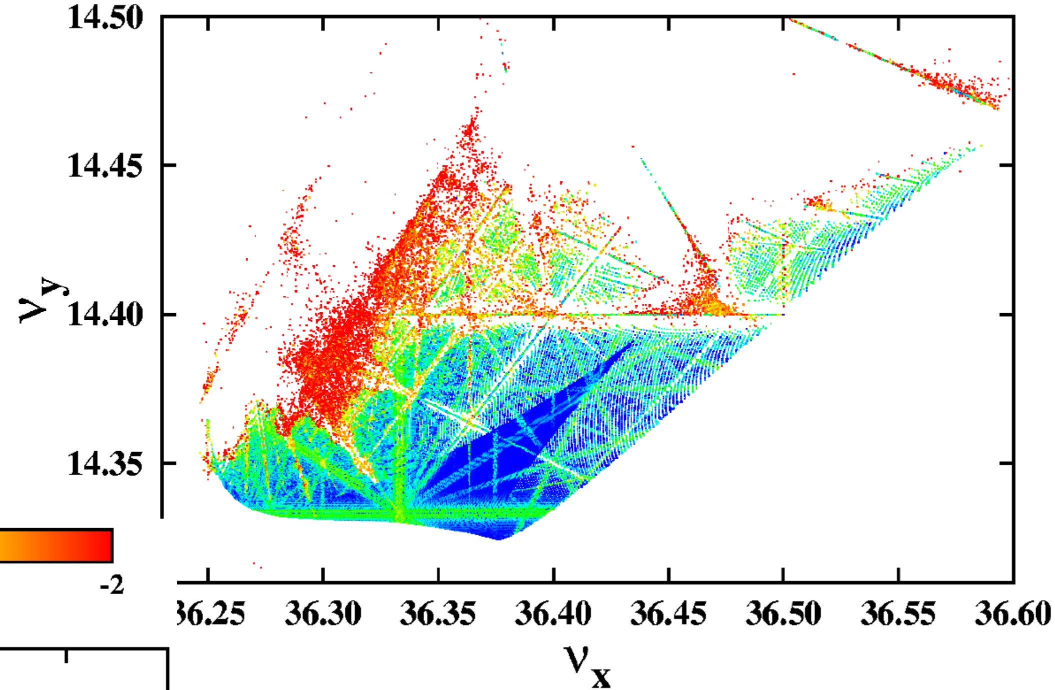

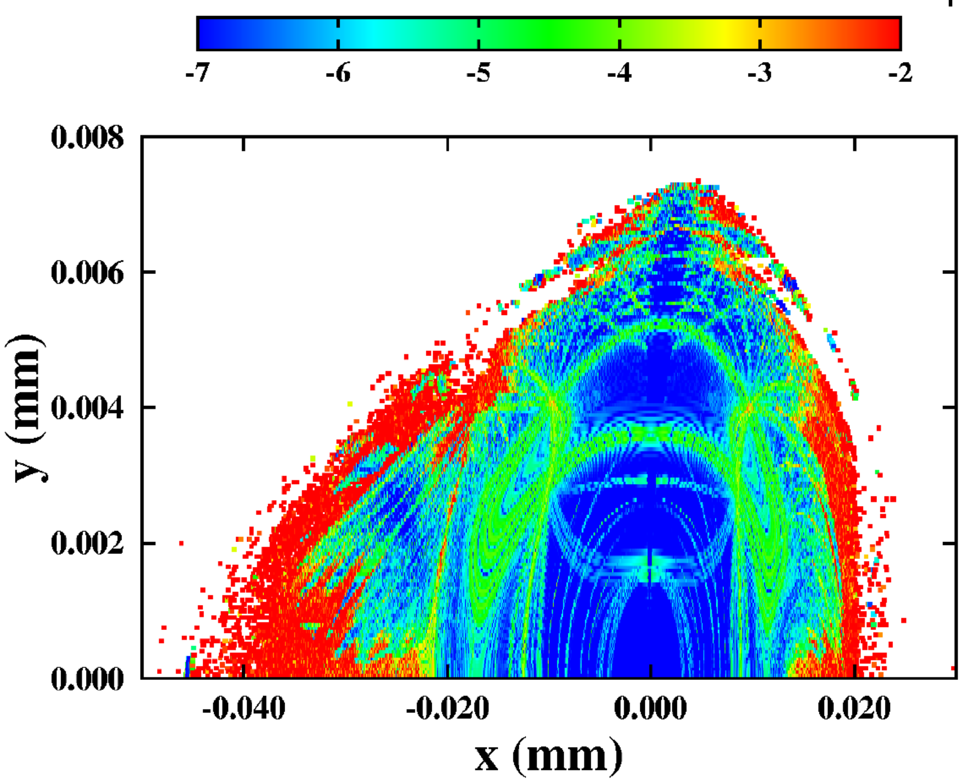

- Resonances appear as distorted lines in frequency space (or curves in initial condition space
- Chaotic motion is represented by red scattered particles and defines dynamic aperture of the machine

Numerical Applications

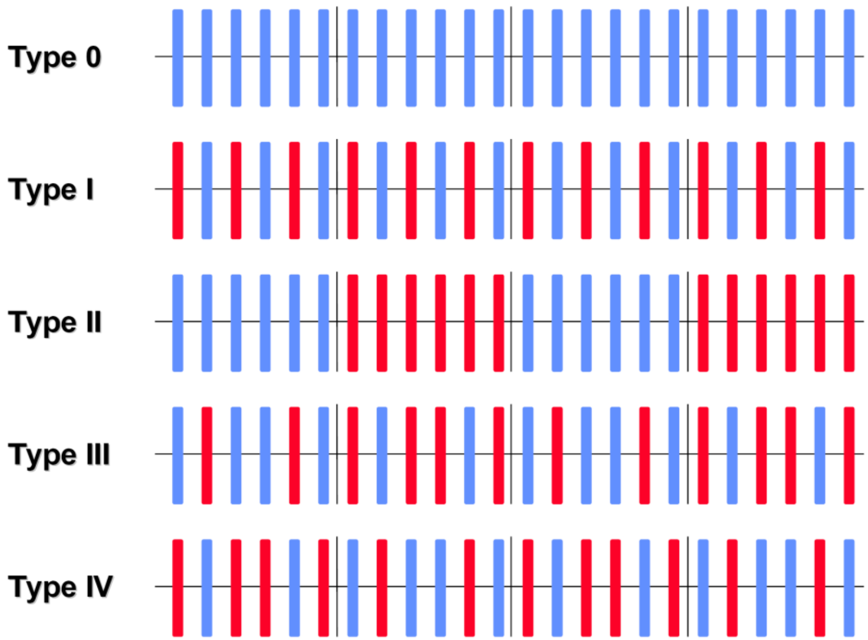

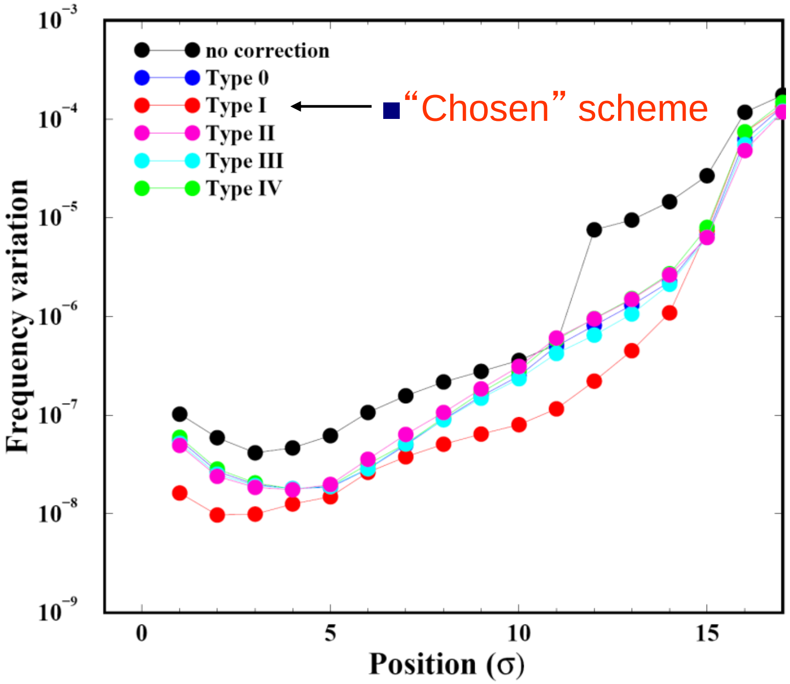

- Comparison of correction schemes for b_4 and b_5 errors in the LHC dipoles
- Frequency maps, resonance analysis, tune diffusion estimates, survival plots and short term tracking, proved that only half of the correctors are needed

Variable	Symbol	Value
Beam energy	E	7 TeV
Particle species	$\cdots$	protons
Full crossing angle	θ_c	300 μrad
rms beam divergence	σ'_x	31.7 μrad
rms beam size	σ_x	15.9 μm
Normalized transv. rms emittance	$\gamma\varepsilon$	3.75 μm
IP beta function	β^*	0.5 m
Bunch charge	N_b	$(1\times 10^{11}-2\times 10^{12})$
Betatron tune	Q_0	0.31

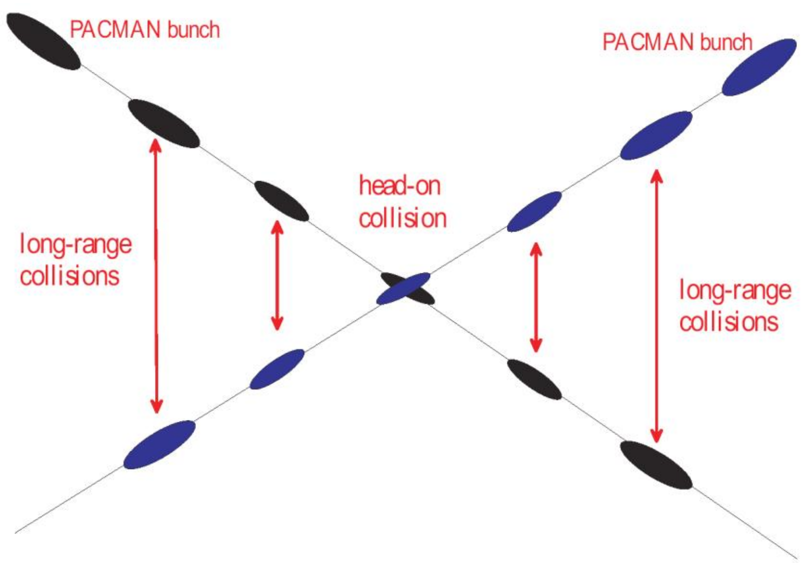

- Long range beam-beam interaction represented by a 4D kick-map

$$\Delta x = -\, n_{par}\,\frac{2r_pN_b}{\gamma}\left[\frac{x'+\theta_c}{\theta_t^2}\left(1-e^{-\frac{\theta_t^2}{2\theta_{x,y}^2}}\right) - \frac{1}{\theta_c}\left(1-e^{-\frac{\theta_c^2}{2\theta_{x,y}^2}}\right)\right]$$

$$\Delta y = -\, n_{par}\,\frac{2r_pN_b}{\gamma}\,\frac{y'}{\theta_t^2}\left(1-e^{-\frac{\theta_t^2}{2\theta_{x,y}^2}}\right)$$

with $\qquad \theta_t \equiv \left((x'+\theta_c)^2+{y'}^2\right)^{1/2}$

Head-on vs Long range interaction

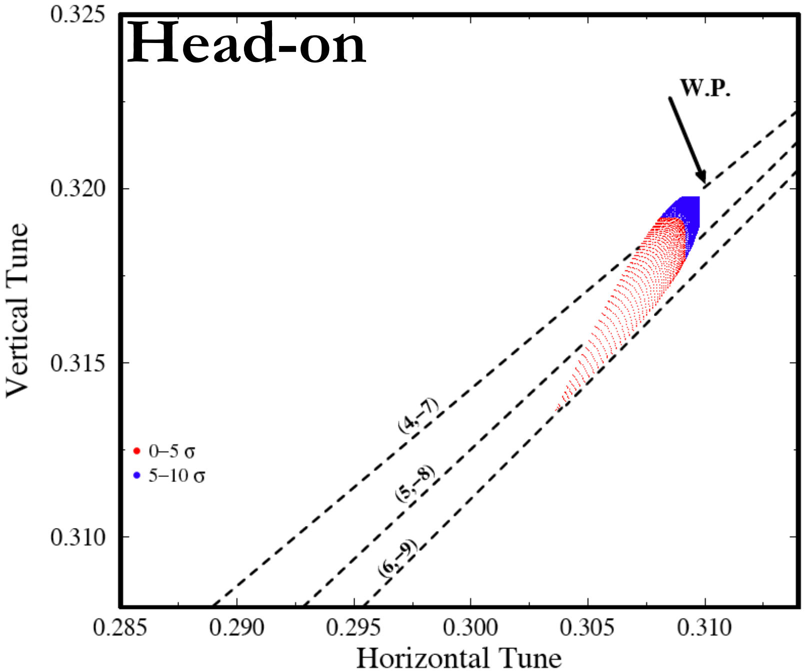

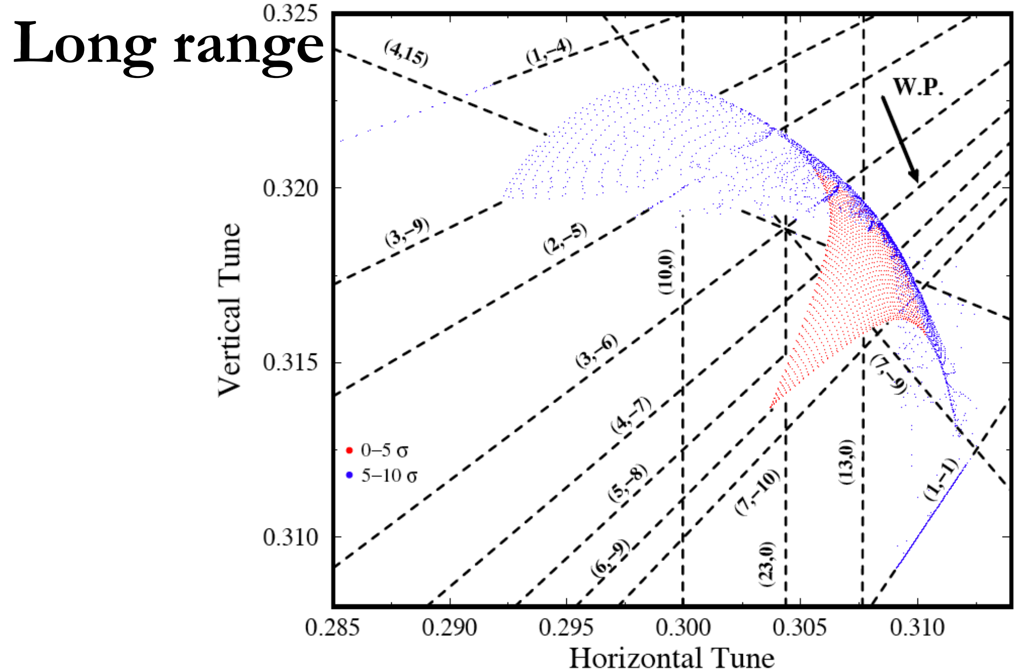

- Proved dominant effect of long range beam-beam effect
- Dynamic Aperture (around 6σ) located at the folding of the map (indefinite torsion)
- Experimental effort to compensate beam-beam long range effect with wires (1/r part of the force) or octupoles

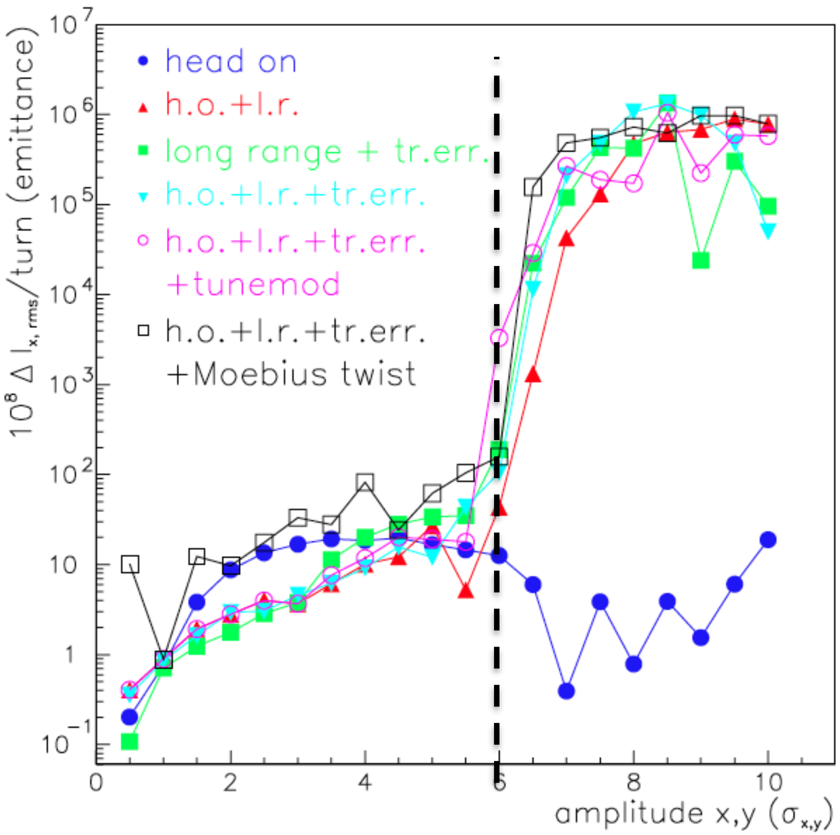

- In the chaotic region of phase space, the action diffusion coefficient per turn can be estimated by averaging over the quasi-randomly varying betatron phase variable as

$$D(J) = \frac{1}{2\pi} \int_0^{2\pi} d\phi \, [\Delta J(\phi)]^2$$

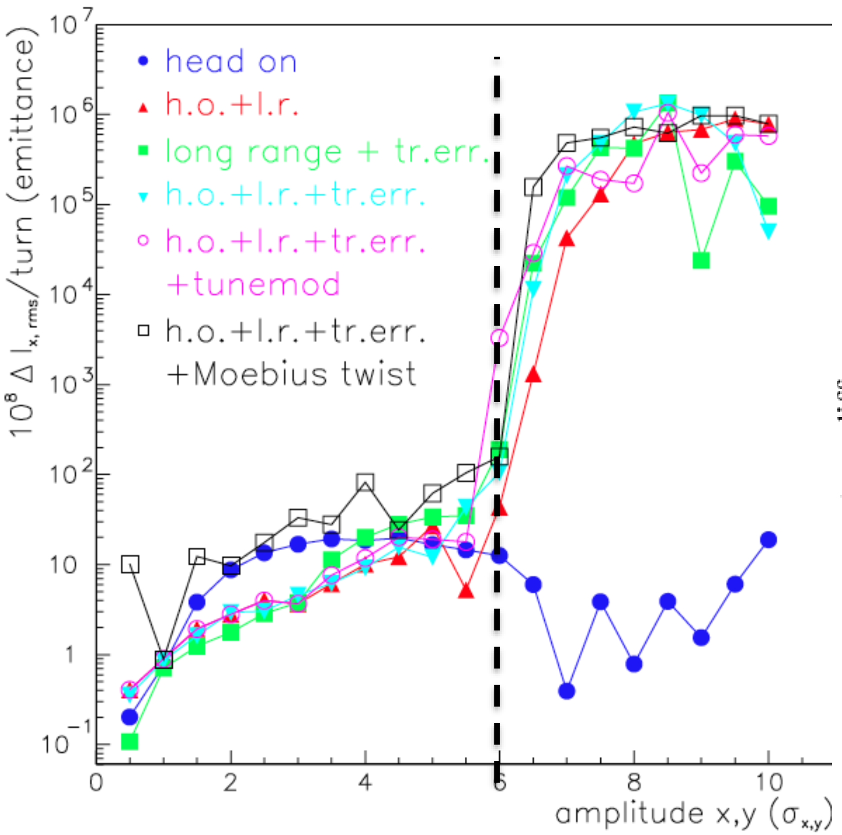

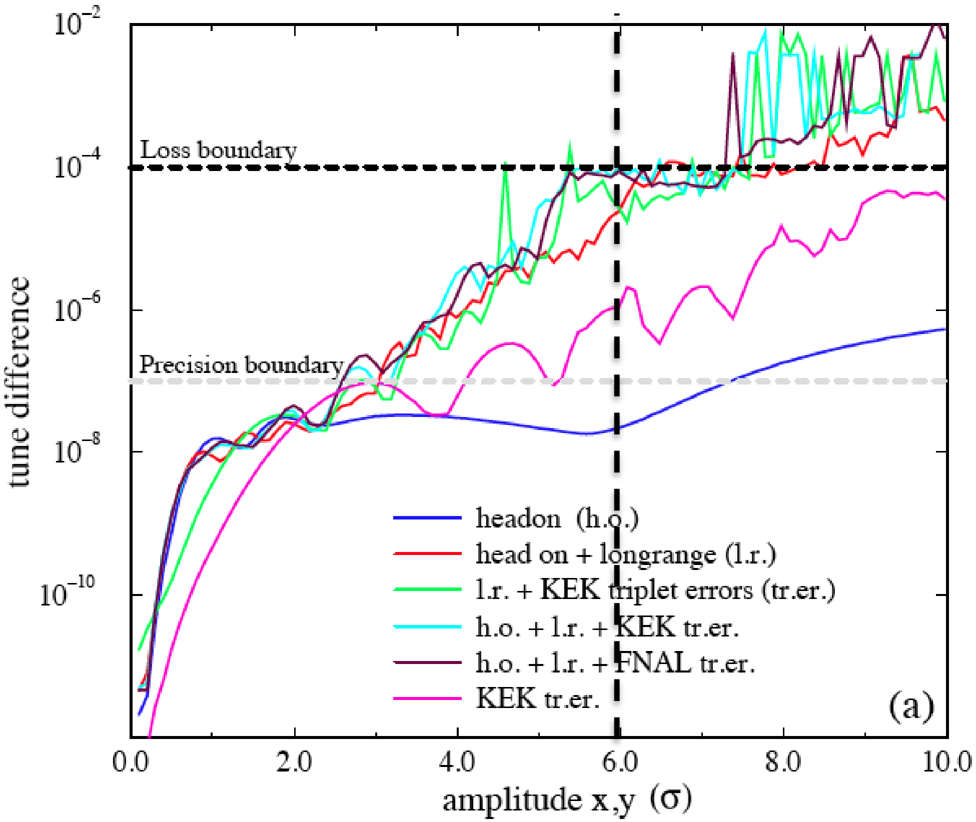

- Very good agreement of diffusive aperture boundary (action variance) with frequency variation (loss boundary corresponding to around 1 integer unit change in 10^7 turns)

Wire compensation

- Current baring wire can **improve DA by 1-2 σ**
- Tests in the LHC during 2017-2018

Without correction | With correction

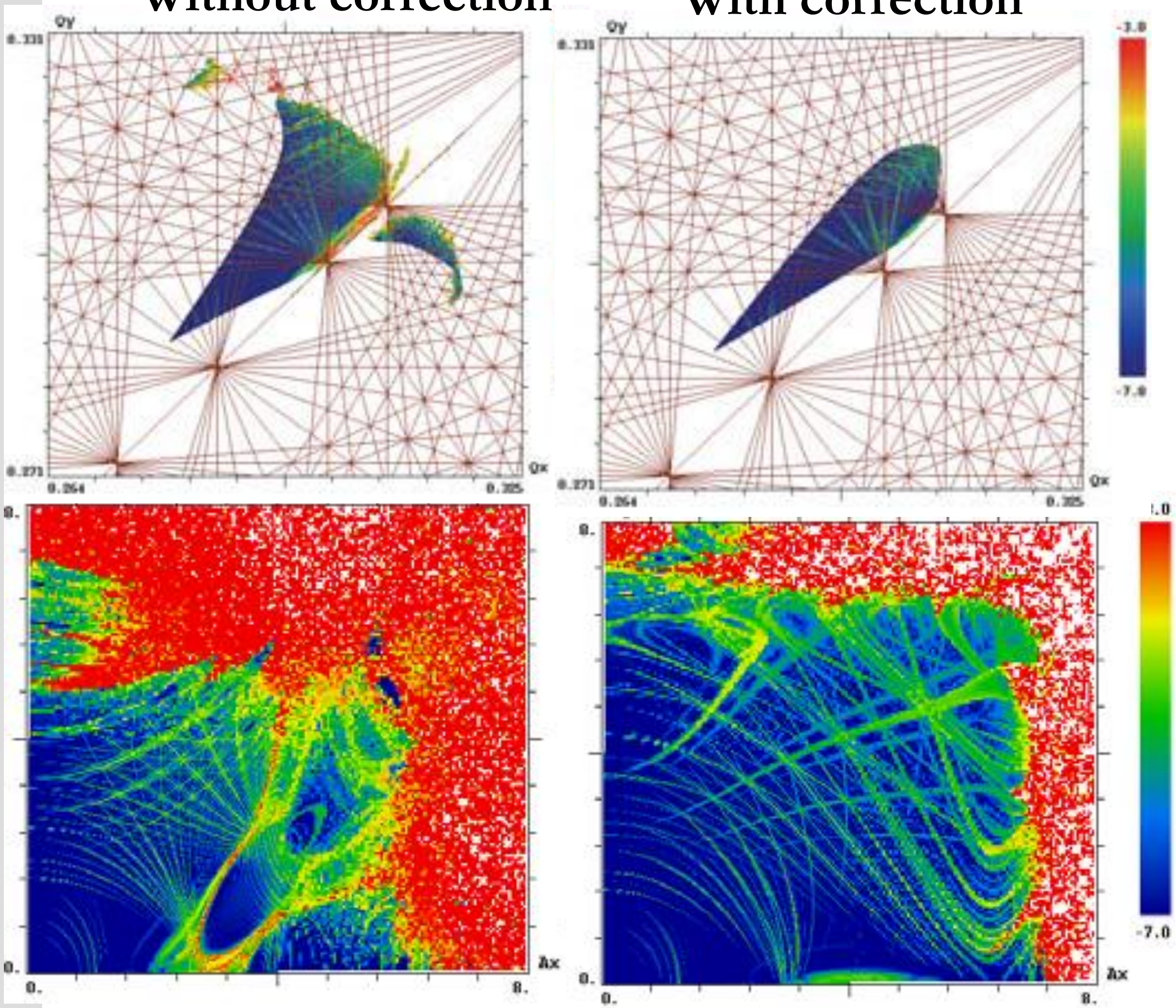

Reduced crossing angle of 450μrad @ 15cm

S. Fartoukh et al., PRSTAB, 2015

K. Skoufaris et al. 2018

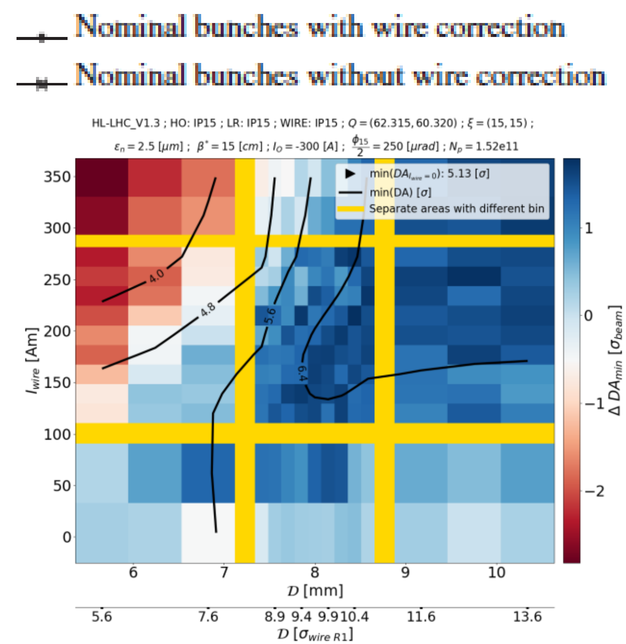

Experimental BBLR compensation

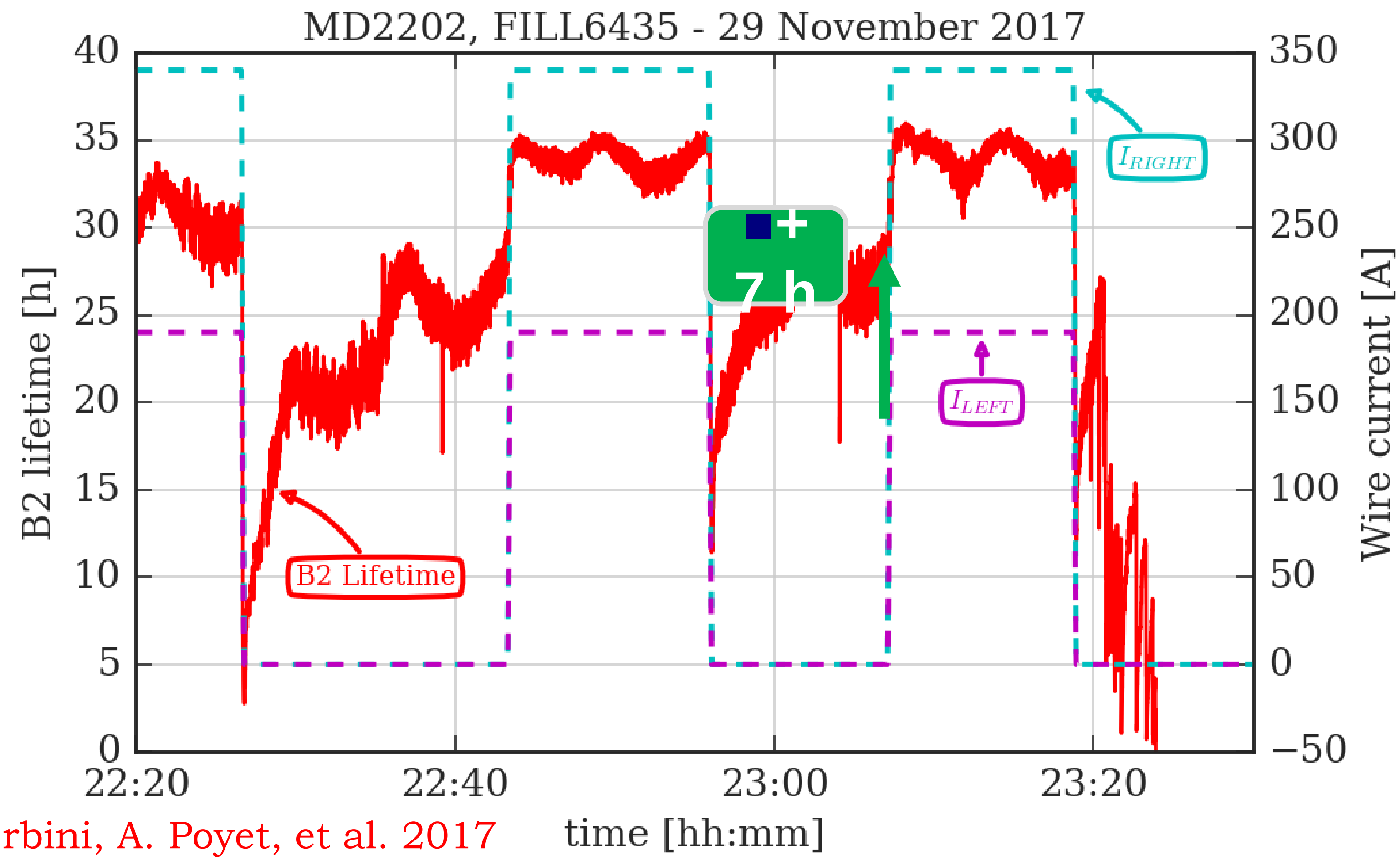

G. Sterbini, A. Poyet, et al. 2017

- Wire current @ 340/190 A and collimator jaw at 5.5 σ_{coll}
- **Compensating effect** of the wires visible on beam **lifetime**

$$\sigma_{EFF} = -\frac{1}{\boxed{\sum_{IP} L_{IP}}} \boxed{\frac{dN}{dt}}$$

Instantaneous luminosity

Intensity loss-rate

- **Compensating effect** of the wires visible on **effective x-section**

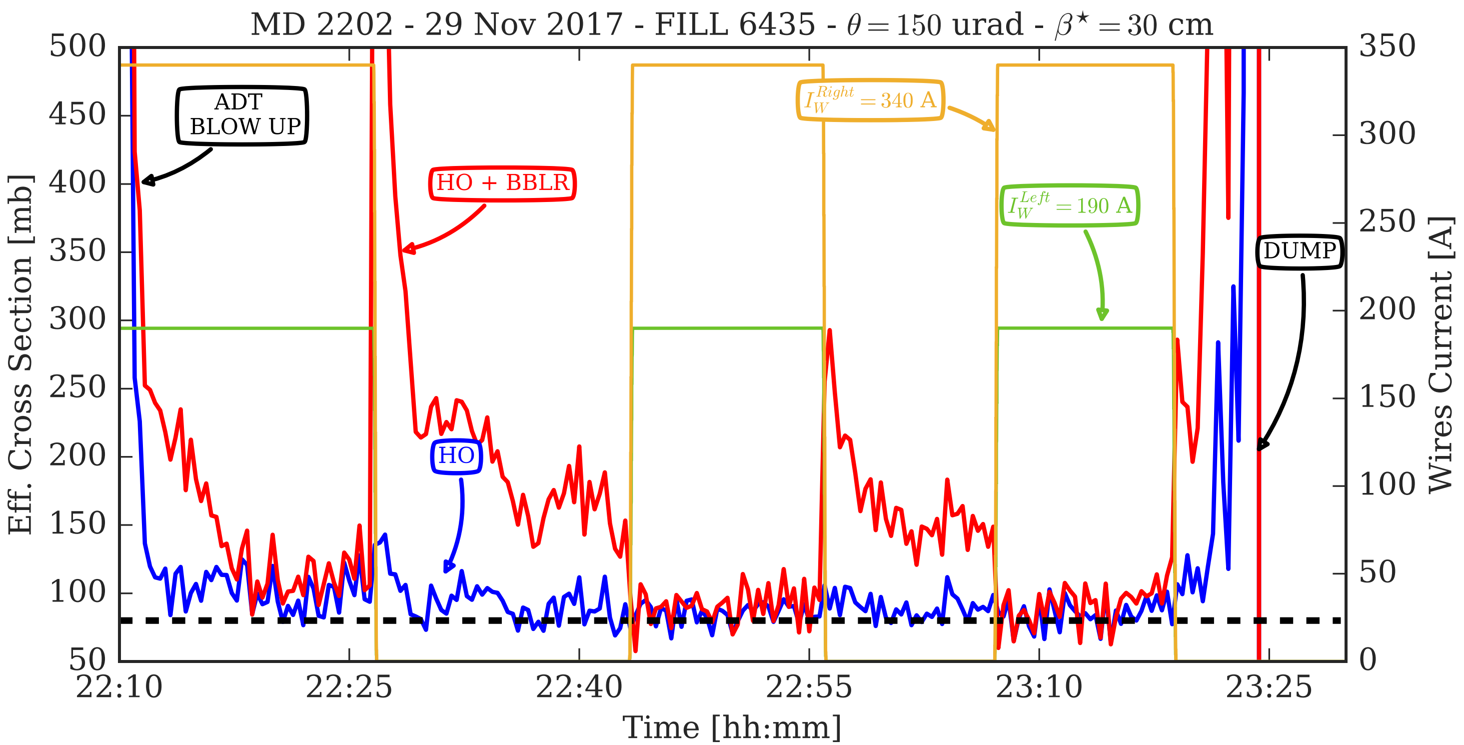

G. Sterbini, A. Poyet, et al. 2017

- Compensation effect visible also with trains and reduced crossing angle!

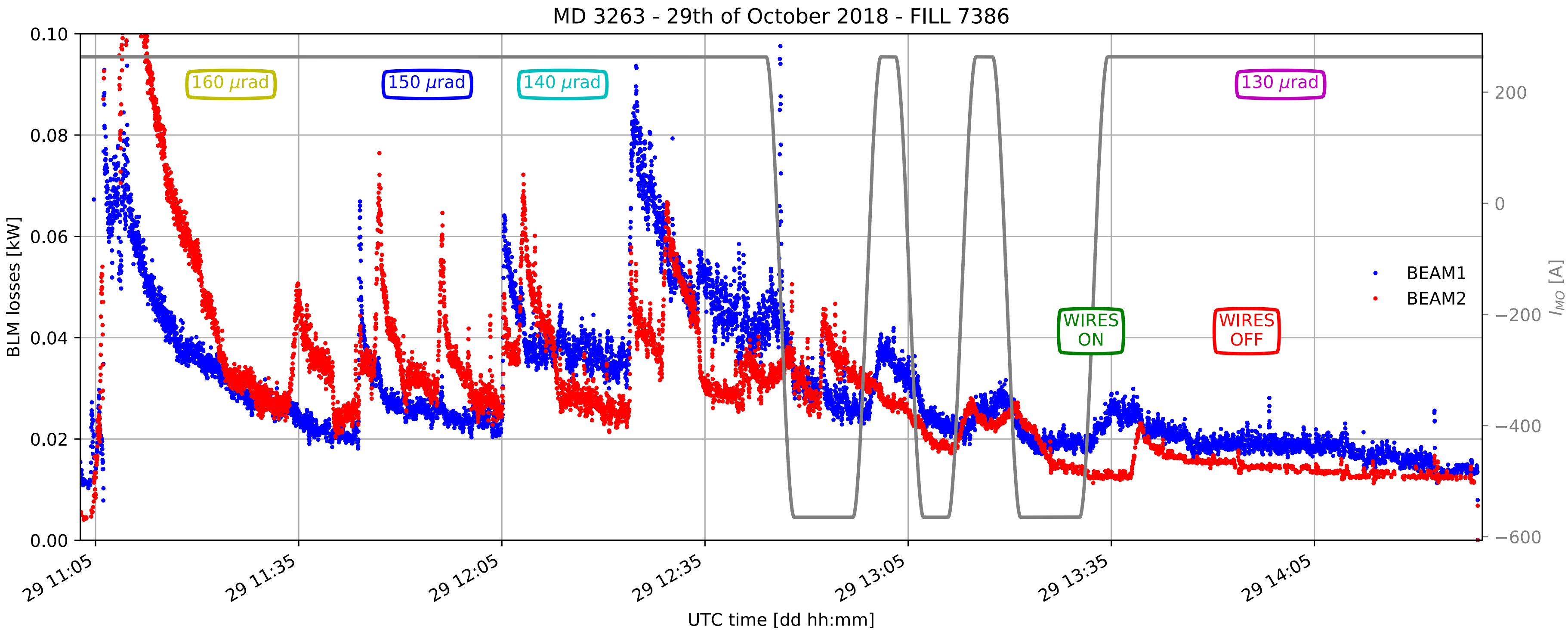

G. Sterbini, A. Poyet, et al. 2017

SABA$_2$C integrator

C. Skokos, YP and J. Laskar, EPAC 2008

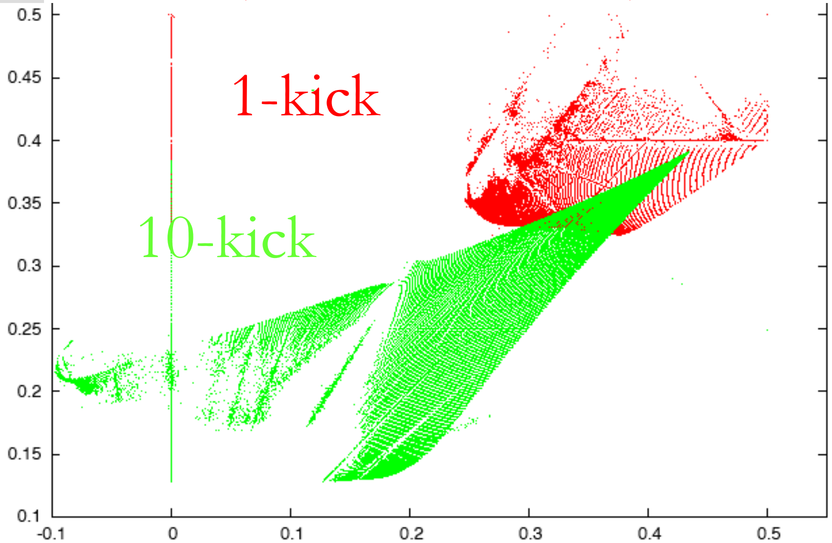

K. Skoufaris et al. IPAC 2018

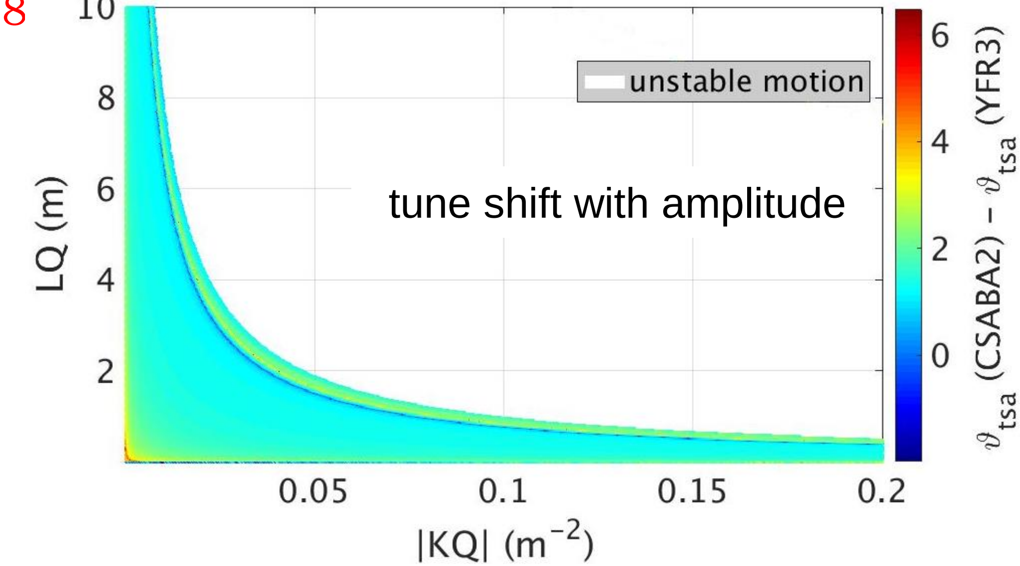

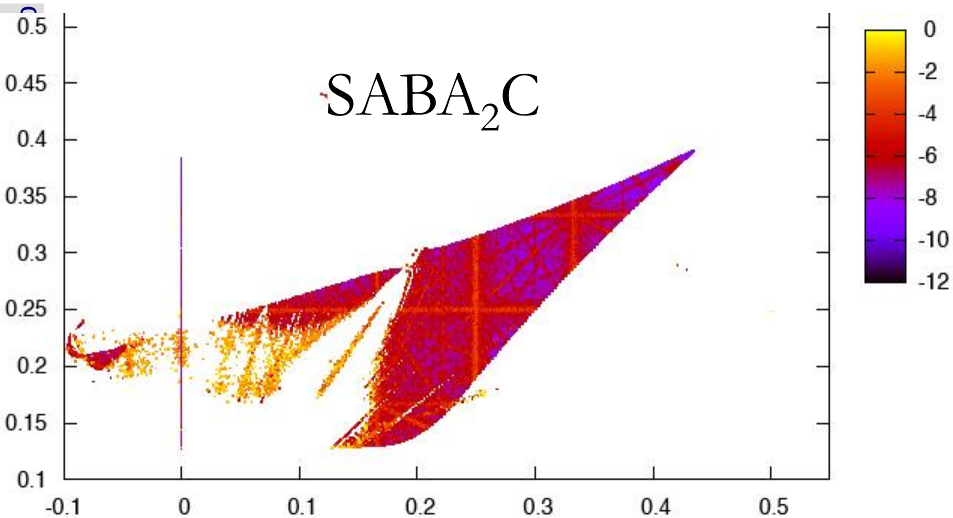

- SABA$_2$C allows symplectic integration with positive steps
- Several orders of magnitude better precision of SABA$_2$C with respect to classical YFR integrator

Magnet fringe fields

- Up to now we considered only transverse fields
- Magnet fringe field is the longitudinal dependence of the field at the magnet edges
- Important when magnet aspect ratios and/or emittances are big

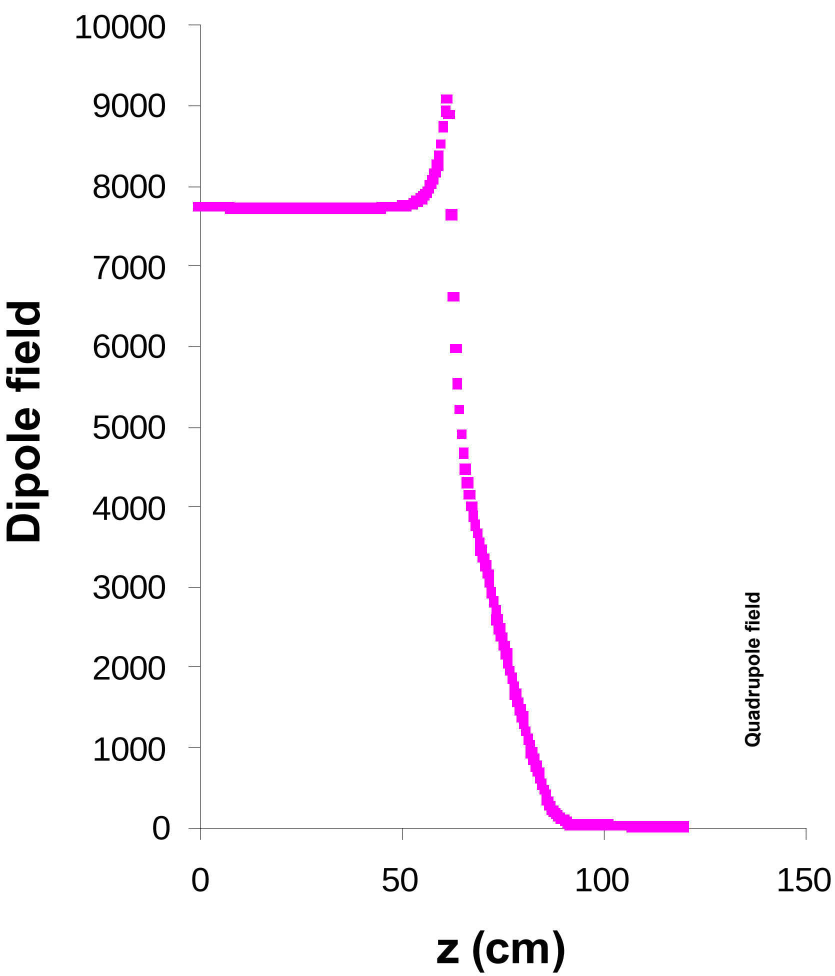

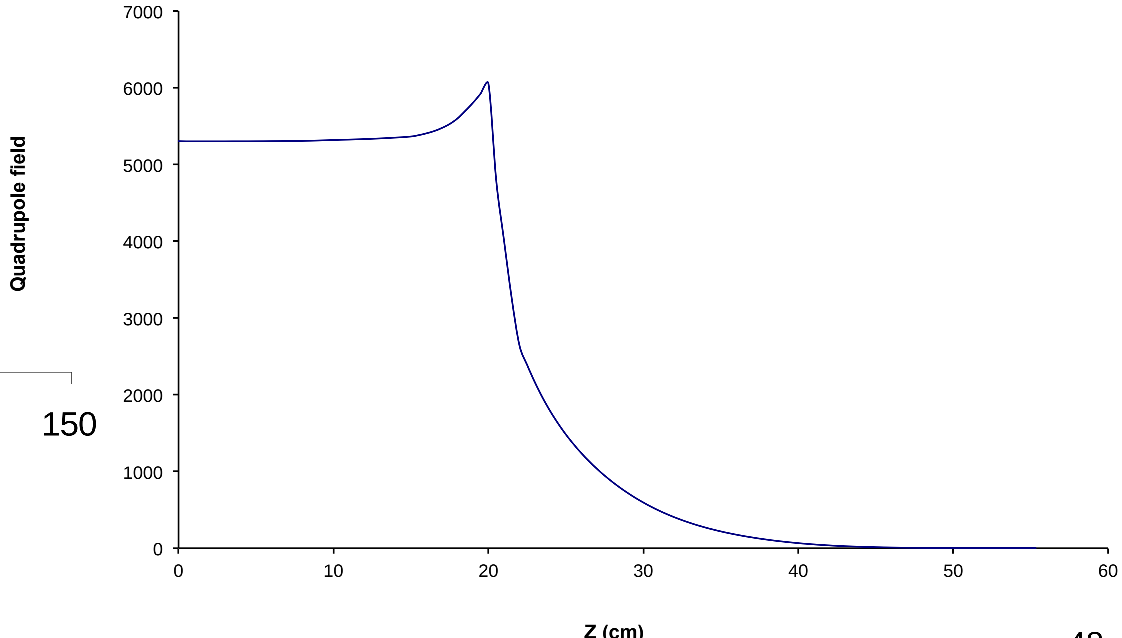

Quadrupole fringe field

General field expansion for a quadrupole magnet:

$$B_x = \sum_{m,n=0}^{\infty} \sum_{l=0}^{m} \frac{(-1)^m x^{2n} y^{2m+1}}{(2n)!(2m+1)!} \binom{m}{l} b_{2n+2m+1-2l}^{[2l]}$$

$$B_y = \sum_{m,n=0}^{\infty} \sum_{l=0}^{m} \frac{(-1)^m x^{2n+1} y^{2m}}{(2n+1)!(2m)!} \binom{m}{l} b_{2n+2m+1-2l}^{[2l]} \quad .$$

$$B_z = \sum_{m,n=0}^{\infty} \sum_{l=0}^{m} \frac{(-1)^m x^{2n+1} y^{2m+1}}{(2n+1)!(2m+1)!} \binom{m}{l} b_{2n+2m+1-2l}^{[2l+1]}$$

and to leading order

$$\begin{aligned} B_x &= y\left[b_1 - \frac{1}{12}(3x^2+y^2)b_1^{[2]}\right] + O(5) \\ B_y &= x\left[b_1 - \frac{1}{12}(3y^2+x^2)b_1^{[2]}\right] + O(5) \\ B_z &= xyb_1^{[1]} + O(4) \end{aligned}$$

The quadrupole fringe to leading order has an octupole-like effect

Magnet fringe fields

- From the hard-edge Hamiltonian

$$H_f = \frac{\pm Q}{12B\rho(1+\frac{\delta p}{p})}(y^3 p_y - x^3 p_x + 3x^2 y p_y - 3y^2 x p_x),$$

the first order shift of the frequencies with amplitude can be computed analytically

$$\begin{pmatrix}\delta\nu_x \\ \delta\nu_y\end{pmatrix} = \begin{pmatrix} a_{hh} & a_{hv} \\ a_{hv} & a_{vv}\end{pmatrix}\begin{pmatrix}2J_x \\ 2J_y\end{pmatrix},$$

with the "anharmonicity" coefficients (torsion)

$$a_{hh} = \frac{-1}{16\pi B\rho}\sum_i \pm Q_i \beta_{xi}\alpha_{xi}$$
$$a_{hv} = \frac{1}{16\pi B\rho}\sum_i \pm Q_i (\beta_{xi}\alpha_{yi} - \beta_{yi}\alpha_{xi})$$
$$a_{vv} = \frac{1}{16\pi B\rho}\sum_i \pm Q_i \beta_{yi}\alpha_{yi}$$

Tune footprint for the SNS based on hard-edge (red) and realistic (blue) quadrupole fringe-field

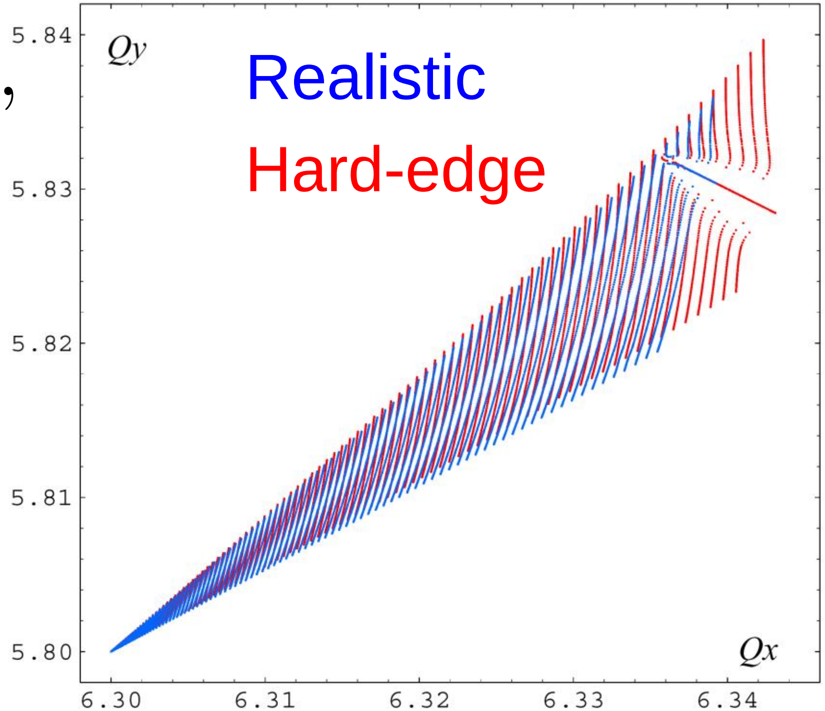

Off-momentum frequency maps

SNS Working Point $(Q_x,Q_y)=(6.4,6.3)$

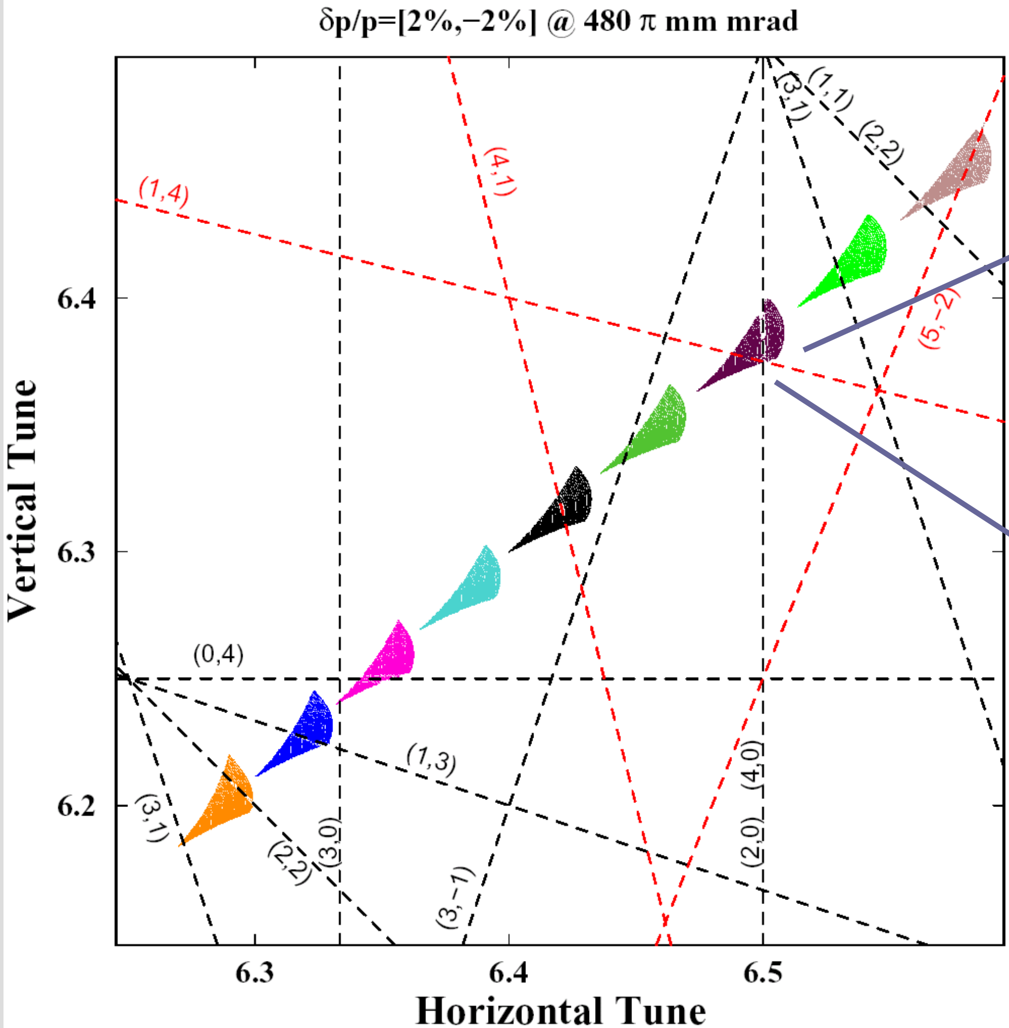

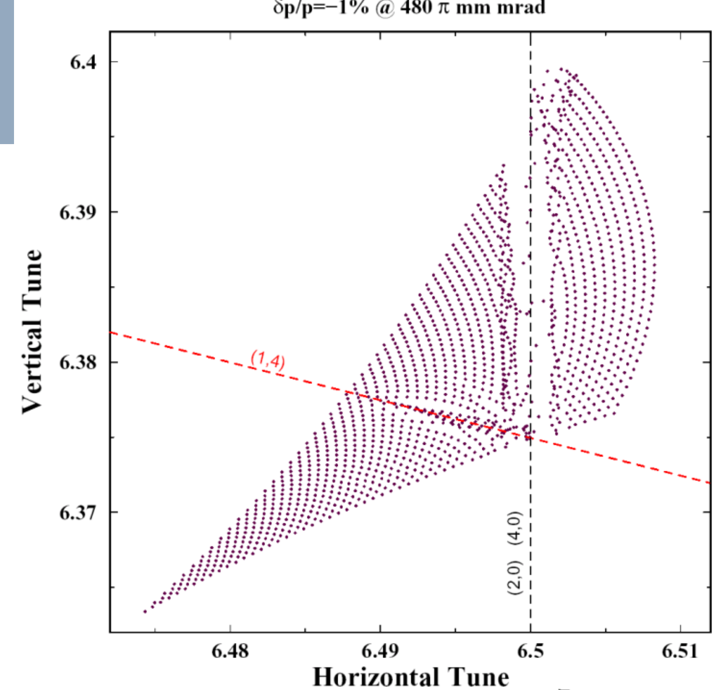

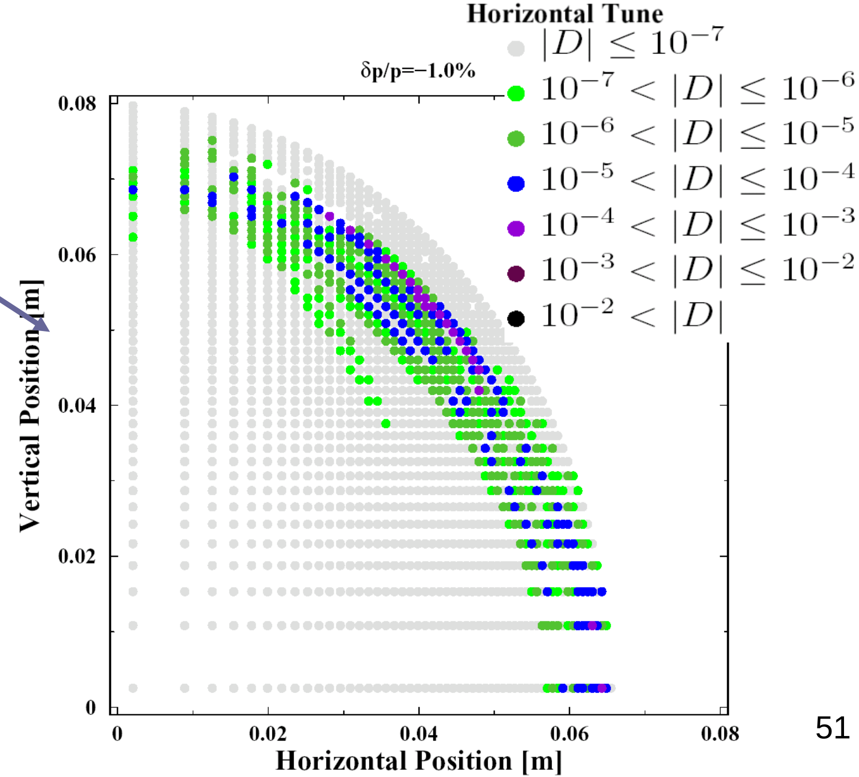

Tune Diffusion quality factor

$$D_{QF} = \langle \frac{|\boldsymbol{D}|}{(I_{x0}^2 + I_{y0}^2)^{1/2}} \rangle_R$$

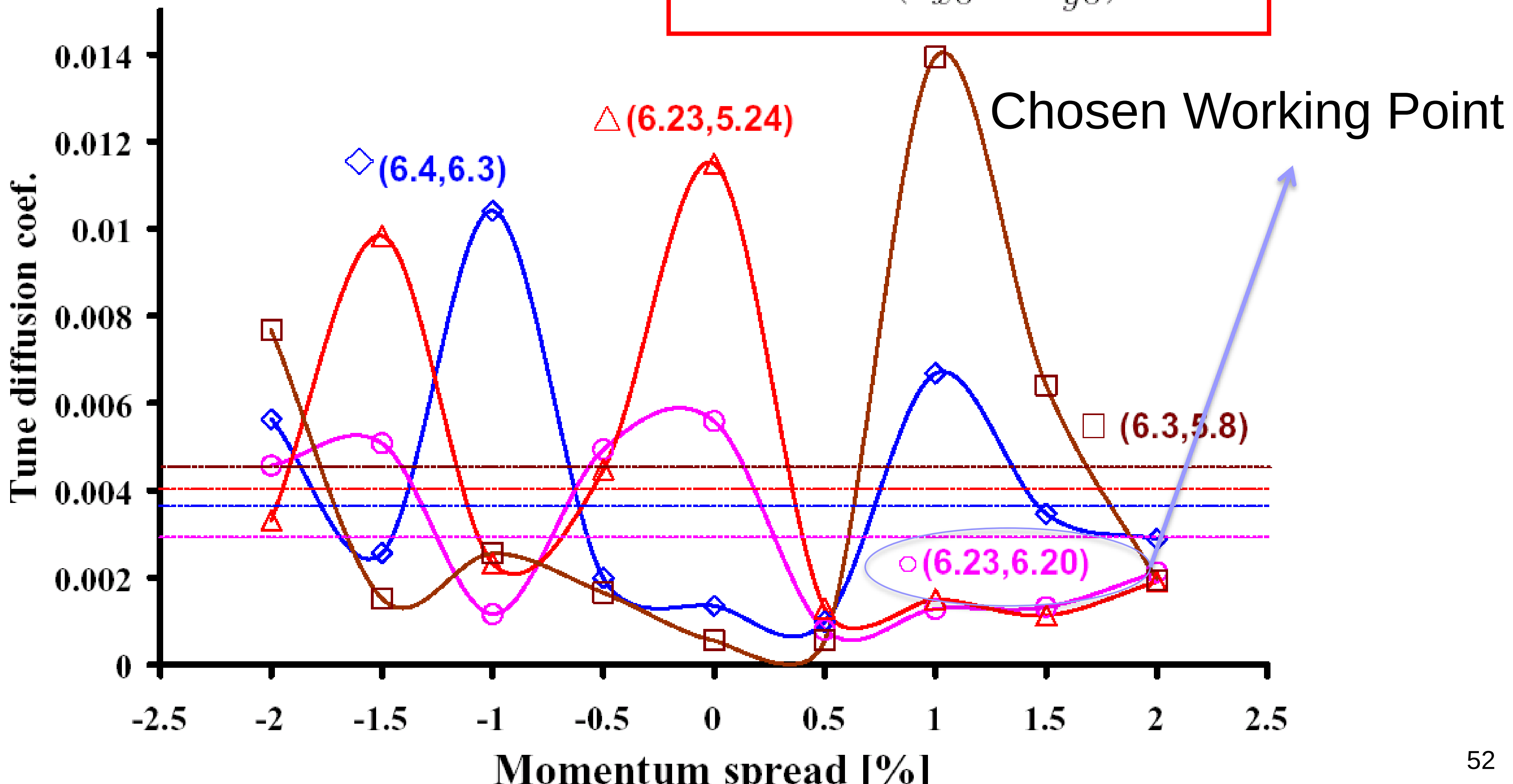

Global Working point choice

- Figure of merit for choosing best working point is sum of diffusion rates with a constant added for every lost particle
- Each point is produced after tracking 100 particles
- Nominal working point had to be moved towards "blue" area

$$e^D = \sqrt{\frac{(\nu_{x,1}-\nu_{x,2})^2 + (\nu_{y,1}-\nu_{y,2})^2}{N/2}}$$

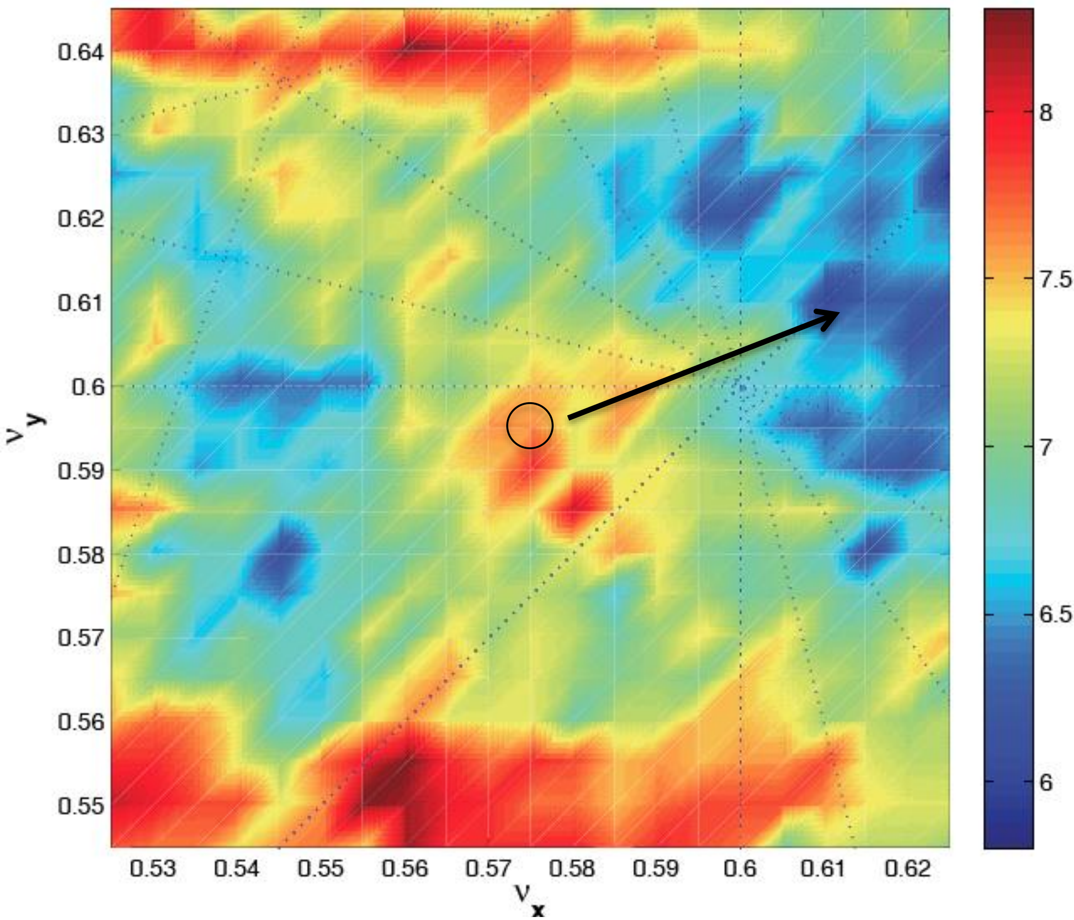

$$WPS = 0.1N_{lost} + \sum e^D$$

Sextupole scheme optimization

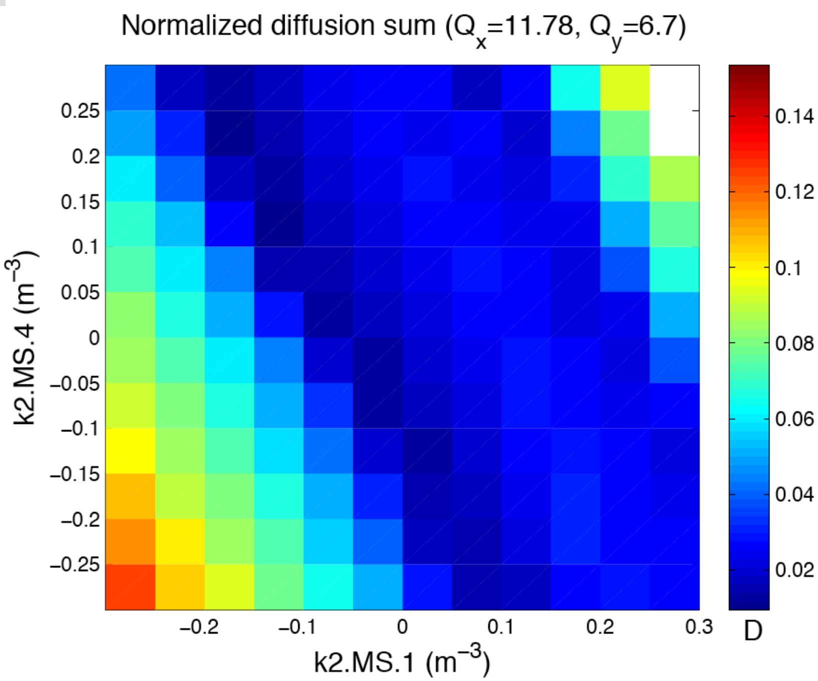

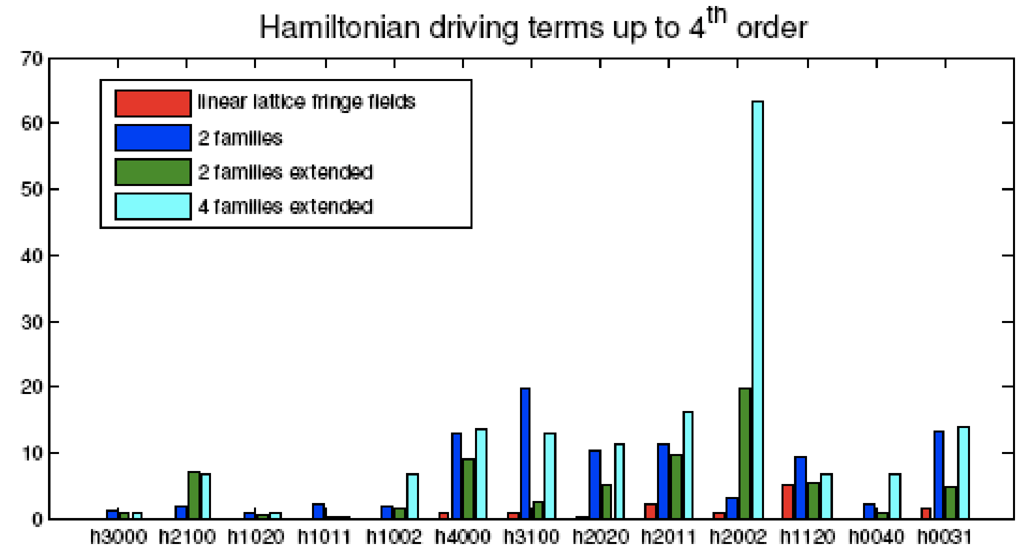

- Comparing different chromaticity sextupole correction schemes and working point optimization using normal form analysis, frequency maps and finally particle tracking
- Finding the adequate sextupole strengths through the tune diffusion coefficient

Frequency Map Analysis with modulation

Frequency maps with space-charge

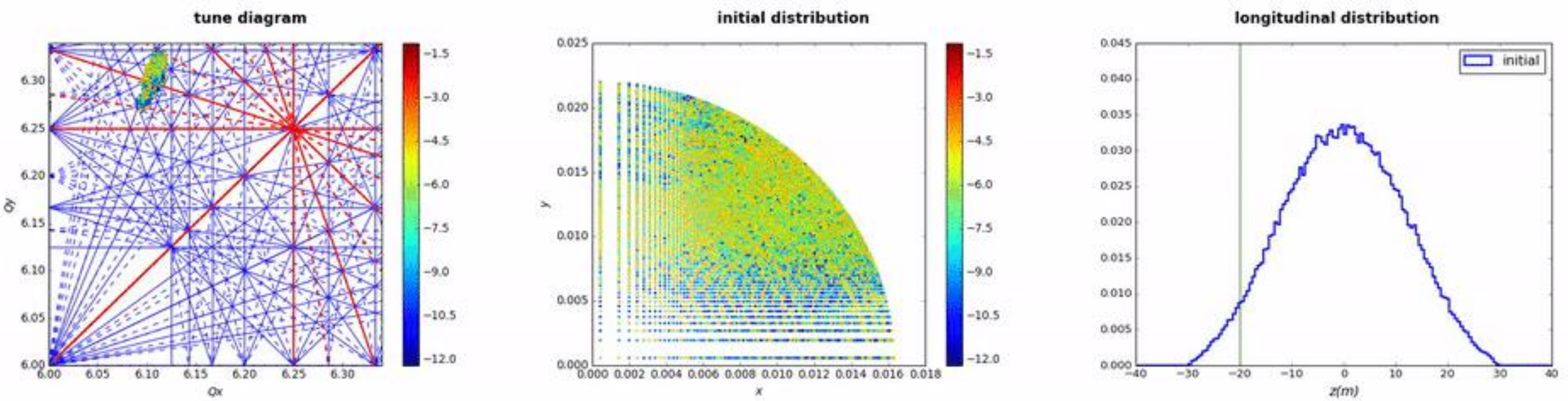

F.Asvesta, et al., 2017

- Evolution of frequency map over different longitudinal position
- Tunes acquired over each longitudinal period
- Particles with similar longitudinal offset but different amplitudes experience the resonance in different manne
- Particles with different longitudinal offset may experienc different resonances

- Quadrupoles of the **inner triplet** right and left **of IP1 and IP5**, **large beta-functions** increase the sensitivity to non-linear effects
- **Resonance conditions**:

S. Kostoglou, et al., 2018

$$aQ_x + bQ_y + c\frac{f_{\text{modulation}}}{f_{\text{revolution}}} = k \text{ for } a, b, c, k \text{ integers}$$

-By increasing the modulation depth, sidebands start to appear in the FMAs

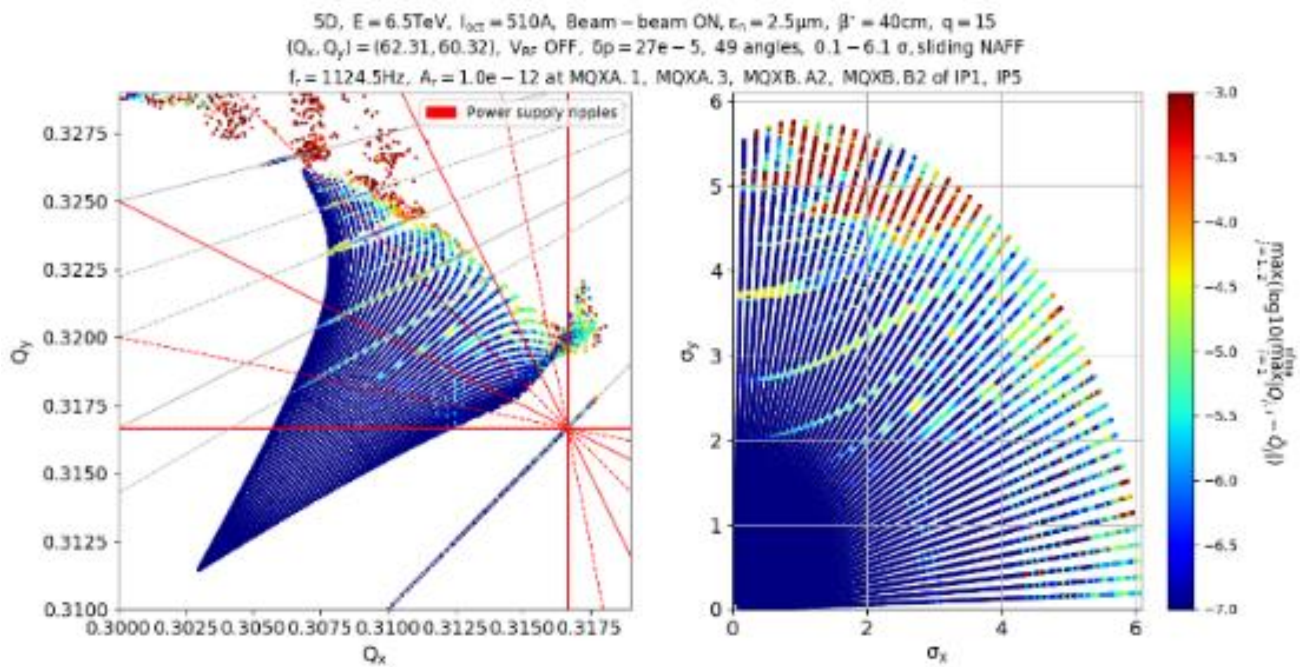

LHC: Power supply ripples

- Quadrupoles of the **inner triplet** right and left **of IP1 and IP5**, **large beta-functions** increase the sensitivity to non-linear effects
- **Resonance conditions**:

S. Kostoglou, et al., 2018

$$aQ_x + bQ_y + c\frac{f_{\mathrm{modulation}}}{f_{\mathrm{revolution}}} = k \text{ for } a, b, c, k \text{ integers}$$

-By increasing the modulation depth, sidebands start to appear in the FMAs

ΔQ=1e-4

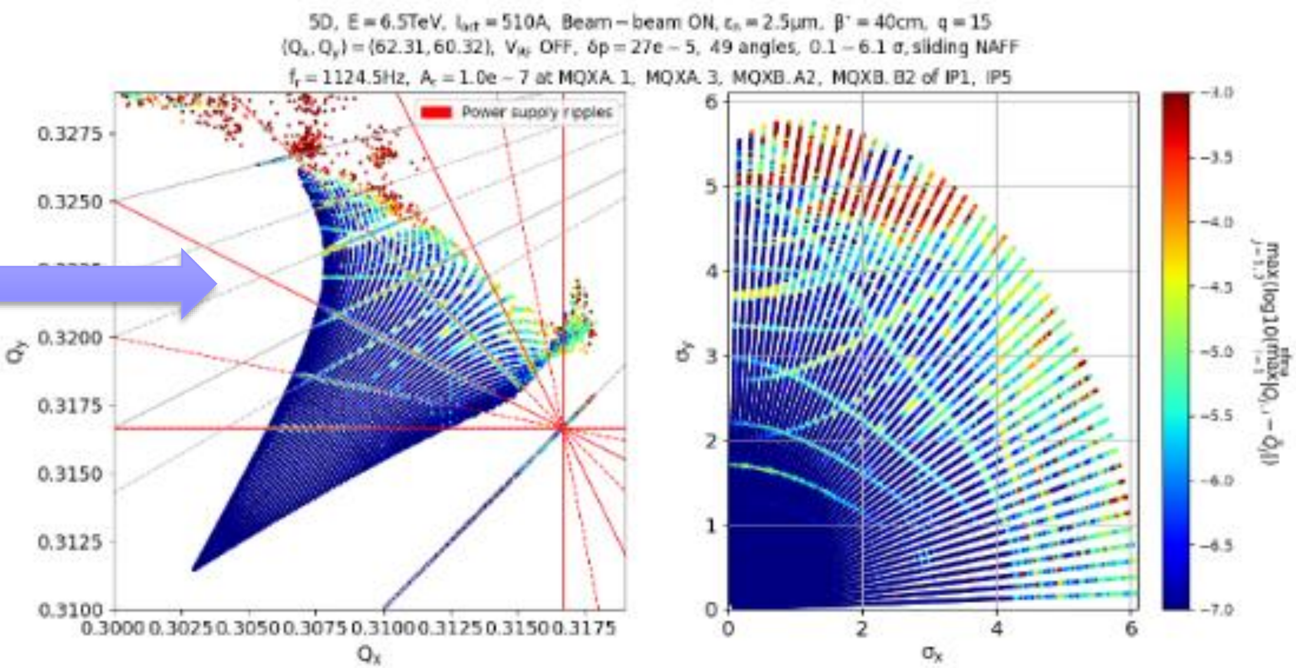

- Scan of different ripple frequencies **(50-900 Hz)**

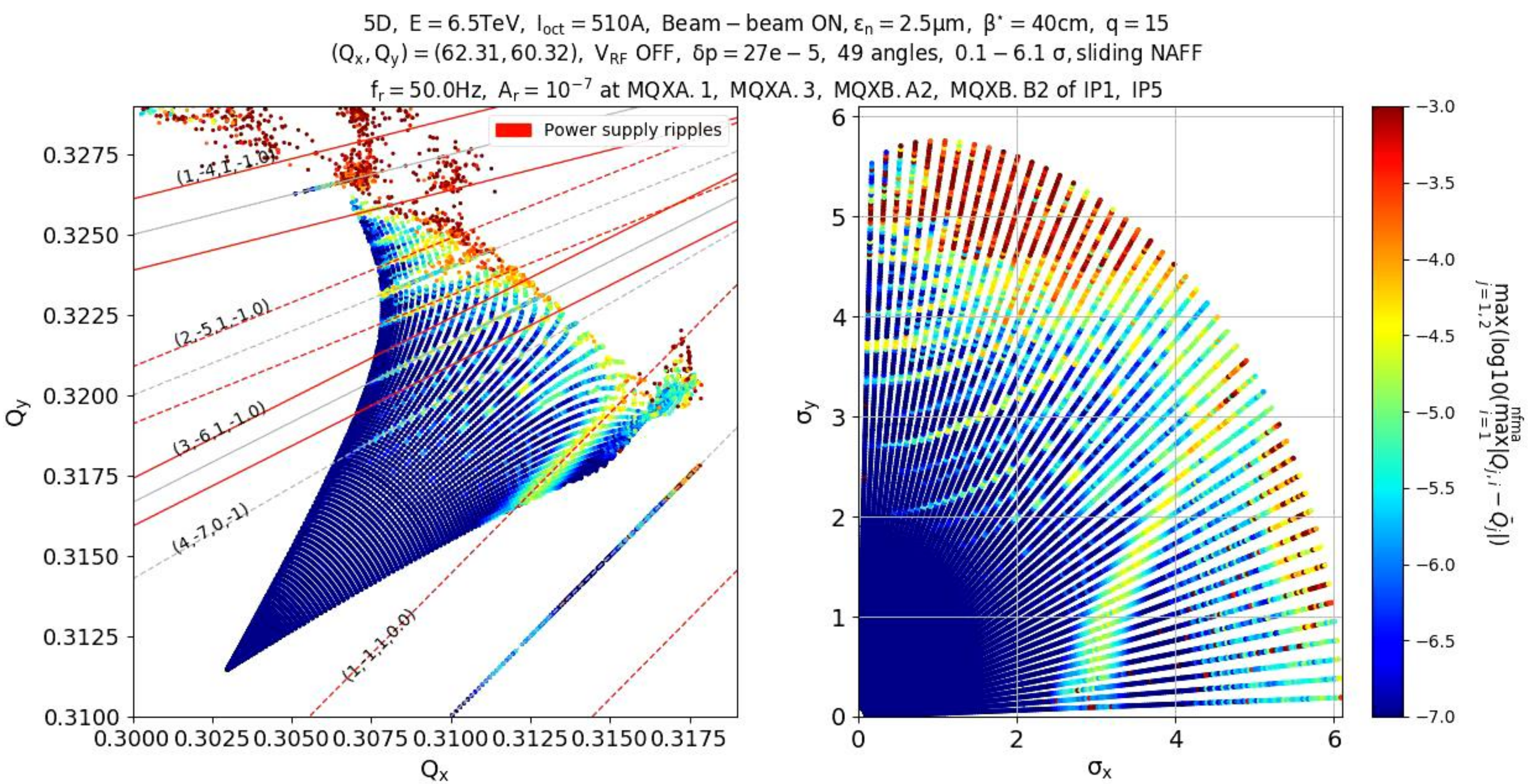

S. Kostoglou, YP et al., 2018

6D FMAs with power supply ripples

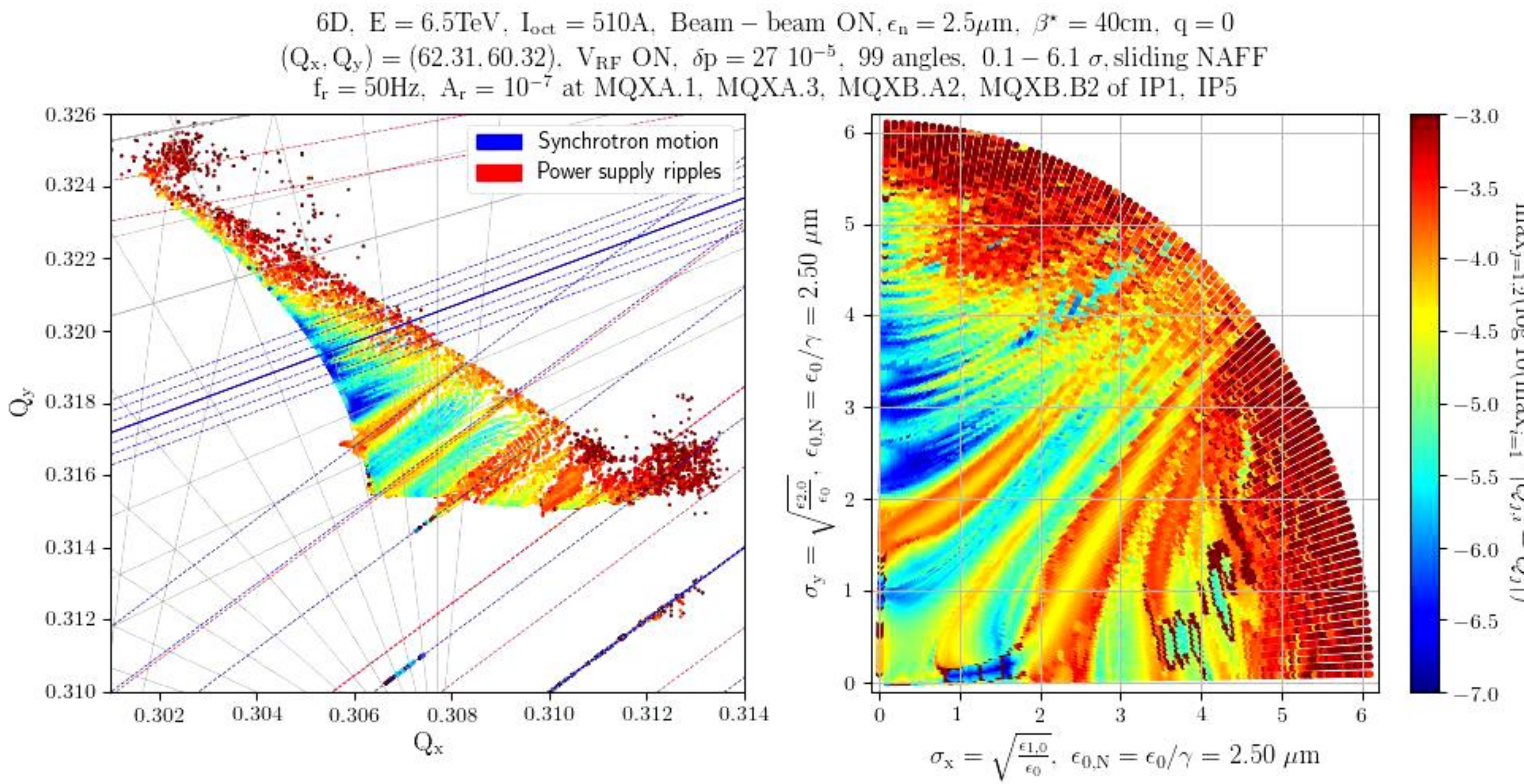

S. Kostoglou, YP et al., 2018

Summary

- Appearance of **fixed points** (periodic orbits) determine **topology** of the phase space
- **Perturbation** of unstable (hyperbolic points) opens the path to chaotic motion
- Resonance can overlap enabling the rapid diffusion of orbits
- **Dynamic aperture** by brute force tracking (with symplectic numerical integrators) is the usual quality criterion for evaluating non-linear dynamics performance of a machine
- **Frequency Map Analysis** is a numerical tool that enables to study in a global way the dynamics, by identifying the excited **resonances** and the extent of **chaotic** regions
- It can be directly applied to **tracking** and **experimental** data
- A combination of these modern methods enable a thorough analysis of non-linear dynamics and lead to a robust design

Acknowledgments

Thanks for the material to F. Antoniou,
F. Asvesta, H.Bartosik, W. Herr,
J. Laskar, N. Karastathis, S.Liuzzo,
L.Nadolski, D. Pellegrini, D.Robin,
C.Skokos, C.Steier, F.Schmidt,
G. Sterbini, A.Wolski, F.Zimmermann

Appendix

- Symplectic integrators with **positive** steps for Hamiltonian systems $H = A + \epsilon B$ with both A and B **integrable** were proposed by McLachan (1995).
- Laskar and Robutel (2001) derived all orders of such integrators
- Consider the formal solution of the Hamiltonian system written in the Lie representation

$$\vec{x}(t) = \sum_{n \geq 0} \frac{t^n}{n!} L_H^n \vec{x}(0) = e^{tL_H} \vec{x}(0).$$

- A symplectic integrator of order n from t to $t + \tau$ consists of approximating the Lie map $e^{\tau L_H} = e^{\tau(L_A + L_{\epsilon B})}$ by products of $e^{c_i \tau L_A}$ and $e^{d_i \tau L_{\epsilon B}}$, $i = 1, \ldots, n$ which integrate exactly A and B over the time-spans $c_i \tau$ and $d_i \tau$
- The constants c_i and d_i are chosen to reduce the error

SABA$_2$ integrator

- The SABA$_2$ integrator is written as

$$\mathrm{SABA}_2 = e^{c_1 \tau L_A} e^{d_1 \tau L_{\epsilon B}} e^{c_2 \tau L_A} e^{d_1 \tau L_{\epsilon B}} e^{c_1 \tau L_A},$$

with $c_1 = \frac{1}{2}\left(1 - \frac{1}{\sqrt{3}}\right)$, $c_2 = \frac{1}{\sqrt{3}}$, $d_1 = \frac{1}{2}$.

- When $\{\{A, B\}, B\}$ is integrable, e.g. when A is quadratic in momenta and B depends only in positions, the accuracy of the integrator is improved by two small negative kicks

$$\mathrm{SABA}_2\mathrm{C} = e^{-\tau^3 \epsilon^2 \frac{c}{2} L_{\{\{A,B\},B\}}} (\mathrm{SABA}_2)\, e^{-\tau^3 \epsilon^2 \frac{c}{2} L_{\{\{A,B\},B\}}}$$

with $c = (2 - \sqrt{3})/24$

- The accuracy of SABA$_2$C is one order of magnitude higher than the Forest-Ruth 4$^{\text{th}}$ order scheme
- The usual "drift-kick" scheme corresponds to the 2$^{\text{nd}}$ order inte

$$\mathrm{SABA}_1 = e^{\frac{\tau}{2} L_A} e^{\tau L_{\epsilon B}} e^{\frac{\tau}{2} L_A},$$

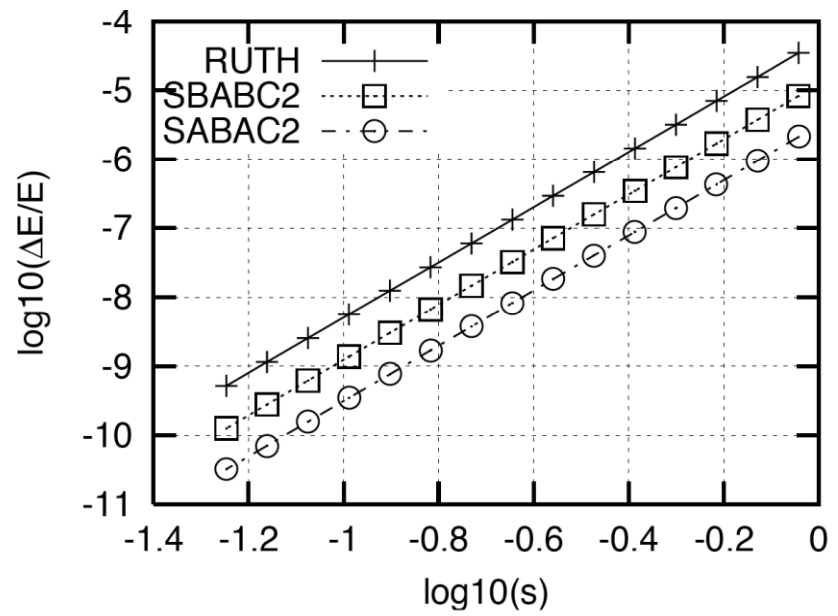

Experimental methods

Experimental frequency maps

D. Robin, C. Steier, J. Laskar, and L. Nadolski, PRL 2000

- Frequency analysis of turn-by-turn data of beam oscillations produced by a fast kicker magnet and recorded on a Beam Position Monitors
- Reproduction of the non-linear model of the Advanced Light Source storage ring and working point optimization for increasing beam lifetime

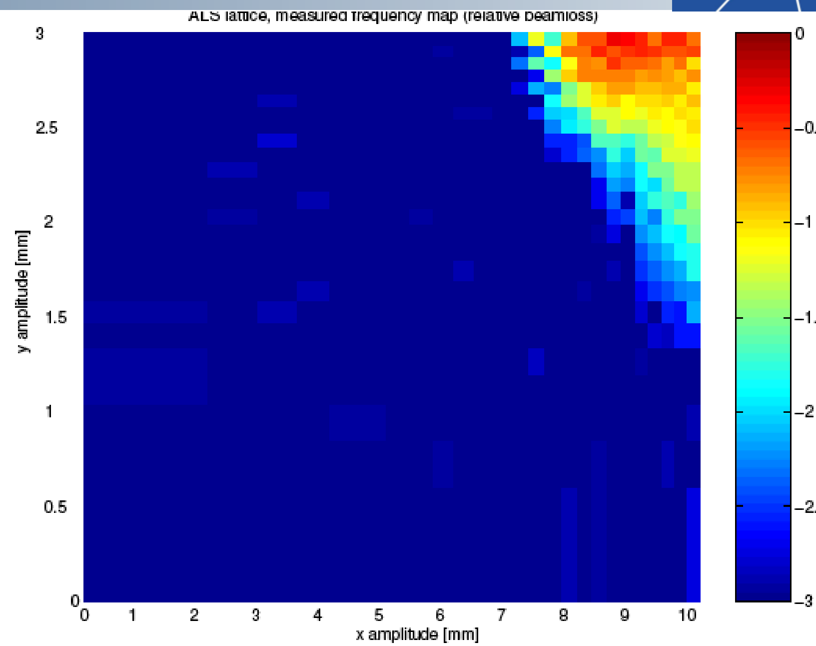

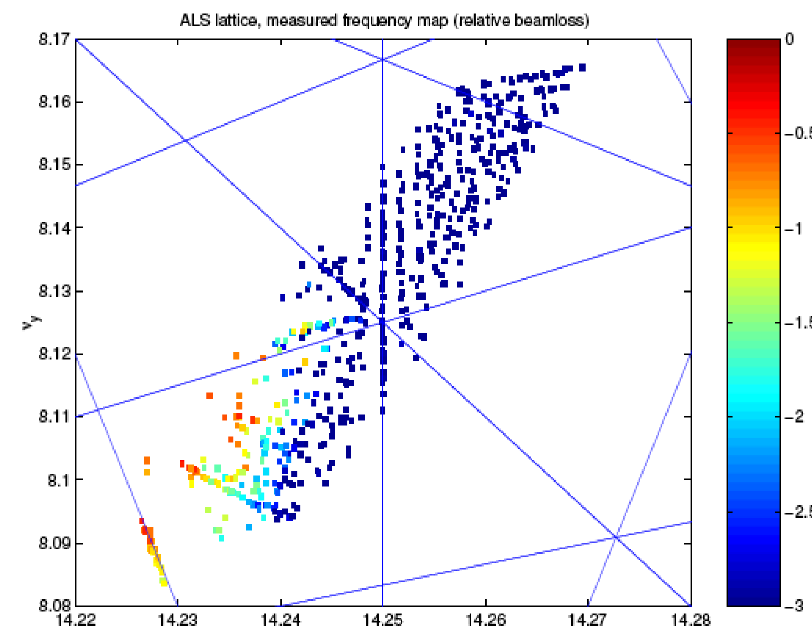

Experimental Methods – Tune scans

- Study the resonance behavior around different working points in SPS
- Strength of individual resonance lines can be identified from the beam loss rate, i.e. the derivative of the beam intensity at the moment of crossing the resonance
- Vertical tune is scanned from about 0.45 down to 0.05 during a period of 3s along the flat bottom
- Low intensity 4-5e10 p/b single bunches with small emittance injected
- Horizontal tune is constant during the same period
- Tunes are continuously monitored using tune monitor (tune post-processed with NAFF) and the beam intensity is recorded with a beam current transformer

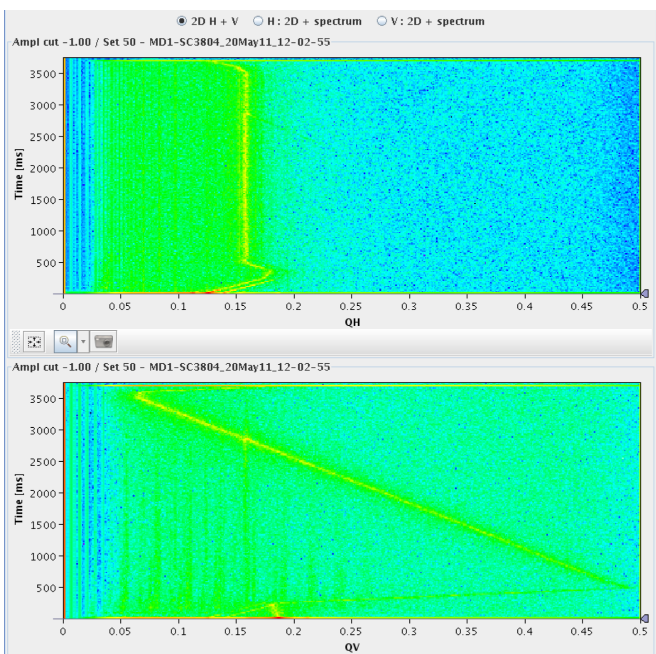

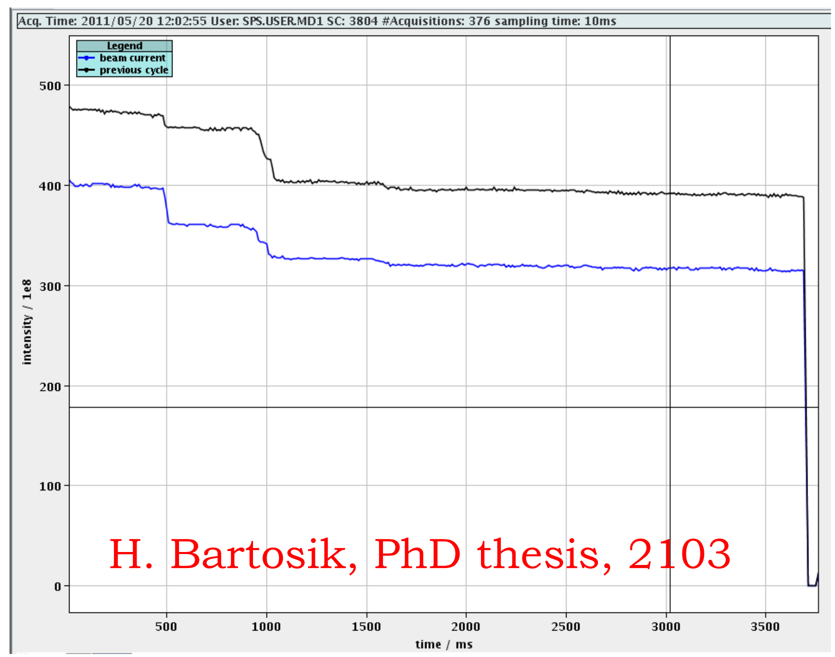

H. Bartosik, PhD thesis, 2103

Tune Scans from the SPS

- Plot the tunes color-coded with the amount of loss
- Identify the dangerous resonances
- Compare between two different optics
- Try to refine the machine model

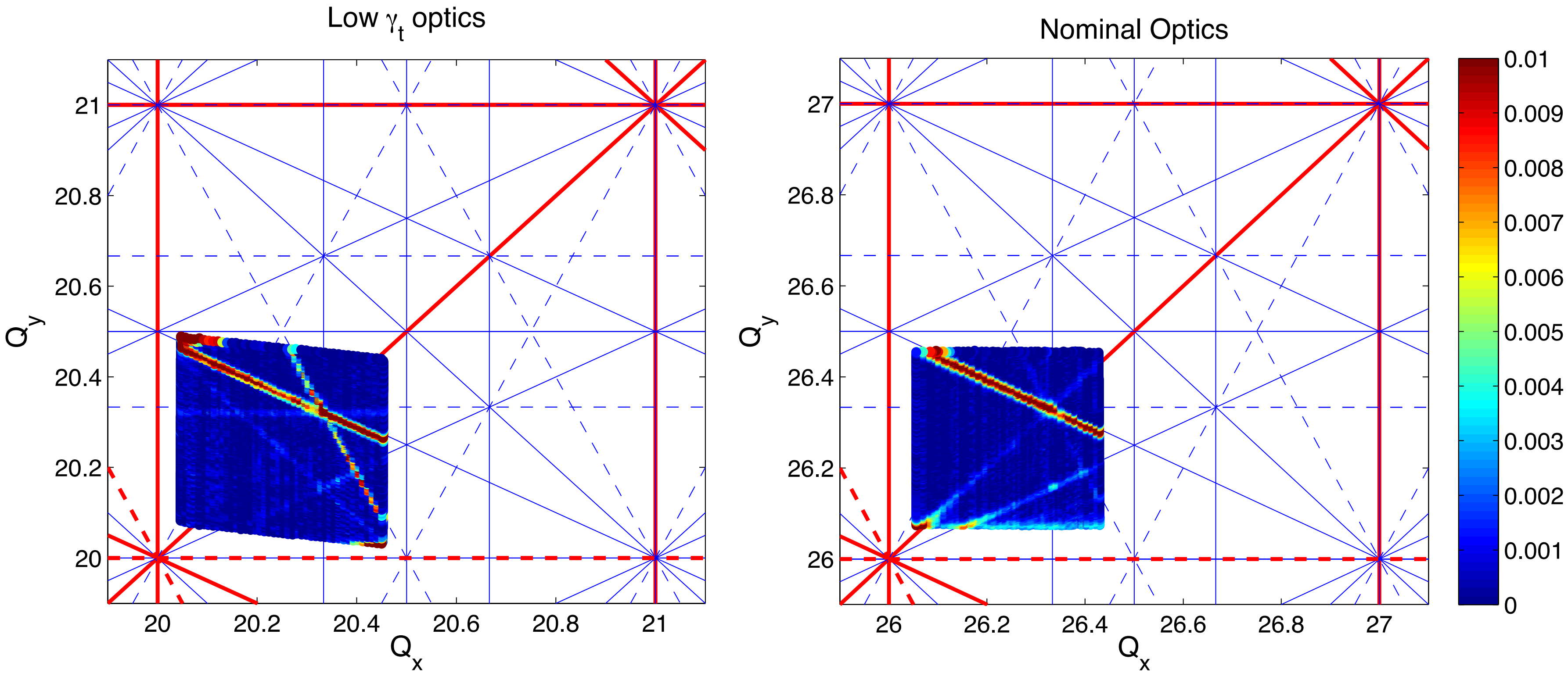

Tune Scans with SC

H.Bartosik

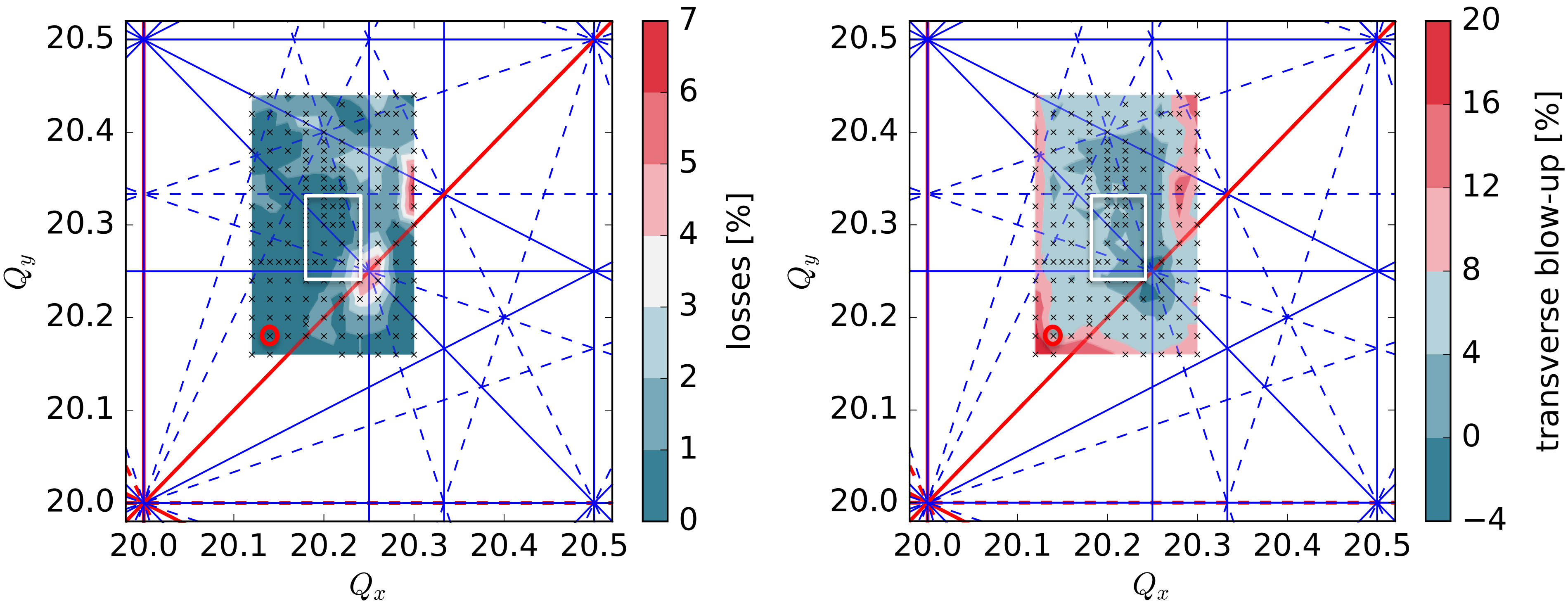

- Limiting resonances for space charge tune spread: (H, V) ~ (0.10, ~0.19)
  - Blow-up at integer resonances as expected
  - Losses for working point close to the Qx + 2Qy normal sextupole resonance (studied in Fix-line experiment with Q26) and around the the 4Qx = 81 normal octupole resonance
- Identified optimum working point area for vertical tune spread of 0.2
  - 20.16 < Qx < 20.23, 20.24 < Qy < 20.33
  - Losses around 0.5% for 3 s storage time on flat bottom